Charles University
Faculty of Science

Study program: Analytical chemistry

Ing. Jiří Trousil

Beating Intracellular Bacterial Infections with Polymeric Nanobead-Based Interventions: Development, Structure Characterization, and Analysis

Doctoral thesis

Supervisor: Mgr. Martin Hrubý, Ph.D., DSc.
Advisor: prof. RNDr. Pavel Coufal, Ph.D.

Prague, 2020

Declaration

The work described in this doctoral thesis was performed at the Institute of Macromolecular Chemistry CAS (IMC CAS) and the Department of Analytical Chemistry (Faculty of Sciences, Charles University) from 2016 to 2020.

I hereby declare that this thesis describes my original work that was performed myself. This work, in whole or in part, has not been submitted to obtain any other degree, diploma or qualification. To the best of my knowledge, I have cited all used sources.

Prague, 6. 5. 2020

Prohlášení

Předkládaná disertační práce byla vypracována na Ústavu makromolekulární chemie AV ČR, v. v. i., a Katedře analytické chemie Přírodovědecké fakulty Univerzity Karlovy v Praze v období 2016 až 2020.

Prohlašuji, že jsem tuto disertační práci vypracoval samostatně, a že jsem uvedl všechny použité informační zdroje a literaturu. Tato práce ani její podstatná část nebyla předložena k získání jiného nebo stejného akademického titulu.

V Praze dne 6. 5. 2020

……...….

Ing. Jiří Trousil

Summary

One hundred years after the discovery of antimicrobials and antibiotics, intracellular bacterial pathogens remain a major cause of global morbidity and mortality. This is due to the complex and intricate ability of these pathogens to undergo intracellular replication while evading host cell immune defense. Bacterial agents such as *Legionella pneumophila*, *Francisella tularensis*, and *Mycobacterium tuberculosis*, as the causative agents of Legionnaires' disease, pulmonary tularemia, and tuberculosis (TB), respectively, contribute to this burden. Moreover, these agents are weaponizable pathogens due to their aerosolizability.

TB represents a global health problem, although a potentially curative therapy has been available for approximately 50 years; this intracellular disease affects approximately 1 in 3 people worldwide, with over 10 million new cases per year and one death every three minutes. TB can usually be treated with a 6- to 9-month course of combined therapy. The necessity of using a cocktail of anti-TB drugs and the long-term treatment schedules required for conventional therapy, however, result in poor patient compliance; therefore, the risk of treatment failure and relapses is higher. Hence, improved drug delivery strategies for the existing drugs can be exploited to shorten the duration of TB treatment and avoid the selection of drug-resistant mutants.

In this context, nanoparticle (NP) technology has emerged as one of the most promising approaches for overcoming the above-listed shortcomings associated with intracellular infection therapies, because of the unique physicochemical properties of NPs. Fabrication of nanocarriers for drug delivery into the lungs, the primary site of TB infection, offers an elegant approach for therapy. Nanobead-based structures follow the route of particulate matter, including intracellular pathogens, and they are preferentially taken up by phagocytes, which further enhances their intracellular targeting. Similarly, the development of effective and safe nanobead-based interventions can be particularly relevant to increasing antibacterial concentrations within the infected site and reducing doses in the systemic circulation, thereby avoiding off-target toxic effects.

Thus, this work utilizes graft and block amphiphilic copolymers to explore self-assembled drug delivery systems for the treatment of intracellular infections. The aim of this thesis was to develop and comprehensively analyze both graft and block copolymer-based assemblies capable of targeting macrophages; nanoarchitecture studies, cytotoxicity analyses and biological system interactions were the main pillars.

By way of a comprehensive analysis based on several complementary instrumental techniques, it was demonstrated that the graft and block polymeric matrices were capable of self-association while providing interesting colloidal behavior, passive macrophage targeting, and low cytotoxicity. Rifampicin-loaded NPs were found to be well tolerated in zebrafish and mice while providing improved anti-TB efficiency. We show that these results are due to improved pharmacokinetic and pharmacodynamic parameters.

Souhrn

Navzdory dostupnosti antibakteriální chemoterapeutické a antibiotické léčby po více než sto let představují bakteriální infekce způsobené vnitrobuněčnými parazity hlavní příčinu globální morbidity a mortality. Je tomu zejména díky schopnosti těchto bakteriálních patogenů unikat dosahu imunitního systému a množit se uvnitř hostitelských buněk (např. makrofágů). Typickými zástupci vnitrobuněčných patogenů jsou *Legionella pneumophila*, *Francisella tularensis* a *Mycobacterium tuberculosis*, původci legionelózy, tularémie a tuberkulózy. Díky tomu, že jsou kultury zmiňovaných patogenů snadno aerosolizovatelné, navíc mohou představovat riziko spadající do kontextu bioterorismu.

Tuberkulózu lze mezi fatálními infekcemi řadit celosvětově na druhé místo hned za HIV, přestože funkční léčba či očkování je k dispozici již přes půl století. Konvenční léčba, založená na několikaměsíčním podávání koktejlu antibiotik, je velice obtížná, jelikož vnitrobuněčně ukryté mykobakterie unikají dosahu obranných mechanismů hostitelských buněk. To spolu s nespolupracujícími pacienty může vést k selekci rezistentních kmenů.

Jedním z možných přístupů je využití nanočástic, které představují nástroj cílení antibiotik do hostitelských buněk a tím podstatné zefektivnění terapie. Makrofágy, buňky imunitního systému, jsou totiž ze své podstaty vysoce aktivní z hlediska rozpoznávání potenciálně patogenních struktur, jako jsou právě bakterie. Benefitem tohoto fenoménu je tak schopnost pohlcovat i umělé a vysoce definované nanostruktury nesoucí účinnou látku.

Cílem této práce proto bylo využít amfifilní roubované a blokové kopolymery a v kontextu léčby vnitrobuněčných infekcí analyzovat fenomén jejich samouspořádání do nanostruktur s akcentem na detailní analýzu fyzikálně-chemických vlastností, nanoarchitektury, cytotoxicity a interakcí s biologickými systémy *in vitro* a *in vivo*.

Předkládaná dizertační práce demonstruje, že studované amfifilní kopolymery vedou ve vodném prostředí k tvorbě samouspořádaných architektur, přičemž jejich komplexnost a charakter koreluje s vlastnostmi použitých polymerních matric. Instrumentálně rozsáhlá analýza struktury a biorelevantních vlastností prokázala, že diskutované nanoarchitektury jsou pasivně zacíleny do makrofágů, za současné nízké cytotoxicity. Antibakteriální účinnost systému založeného na enkapsulovaném rifampicinu, testovaná *in vitro* a *in vivo*, byla v porovnání s volným léčivem výrazně zvýšená, což potvrdilo i detailní studium farmakokinetiky rifampicinu na myším modelu.

CONTENTS

SPECIFIC AIMS AND PREFACE

LIST OF SYMBOLS AND ABBREVIATIONS

CHAPER 1: THEORETICAL PART

CHAPTER 2: BLOCK COPOLYMER INVESTIGATION

SPECIFIC AIMS AND PREFACE

Research Motivation and Scientific Rationale

The basis for my research originally stemmed from my three passions/research interests of analytical chemistry, nanoscience and infection biology.

Infectious diseases continue to represent a global health problem. Geographically, they spread much faster now than at any time in history, as reported by the World Health Organization (WHO). Similarly, the spread of drug-resistant infections highlights the global vulnerability and interrelatedness of health systems and the challenges of health equity. Thus, improvements in rapid diagnostics and novel strategies for the treatment of infectious diseases are urgently required and remain necessary to prevent their global spread, allow economic development, and increase the equity of health.

Tuberculosis (TB) remains the leading cause of preventable death in the world, although a potentially curative therapy has been available for approximately 50 years. This is because the host-pathogen relationship is highly adapted. Moreover, emerging resistance and inadequate medical care in most of the world have resulted in widespread disease. TB kills 1.5 million people per year; it is reported that one-third of the world's population is latently infected.

The standard therapy regimen is based on an intensive phase of 2 months of treatment with first-line anti-TB drugs, followed by a 4-month continuation phase. This anti-TB therapy, however, faces challenges because of the pathogenesis of this kind of intracellular bacteria: they are able to hide, reside, and proliferate within the host cells. Moreover, systemic administration of anti-TB drugs leads to dissemination and off-target toxicities. Hence, there is an unmet need for new strategies addressing these shortcomings.

Nanoparticle (NP) technology has emerged as one of the most promising approaches for overcoming the above-listed complications associated with intracellular infections due to the interesting properties of NPs. Utilizing nanobead-based interventions for drug delivery into the lungs, the primary site of TB and other pulmonary infections, has been suggested as an elegant approach. Each novel drug delivery system and nanobead-based intervention, however, requires robust structure characterization and behavior analysis with an emphasis on biological systems, as all the NP properties govern the *in vitro* and *in vivo* efficiency. This kind of testing and characterization includes a broad range of analytical approaches, which brings us to the relation to analytical chemistry.

Analytical chemistry obtains, processes and communicates information about the composition and structure of matter. In other words, it determines *what* matter is and *how much* of it exists. The recent pillar questions of analytical chemistry, however, transcend to other characteristics; they deal with questions of *where* matter is, *when* matter is, and in *which form* matter exists. These are the parameters researchers dealing with drug delivery systems and nanobead-based interventions need to consider. Altogether, answers to the abovementioned pillar questions precede processes that can be called biorelevant analysis, *i.e.*, one of the essential aspects of this work.

Specific Aims

Given the background described above, this doctoral thesis is motivated by the goal of developing, engineering, and analyzing functional nanobead-based systems capable of passively targeting eukaryotic cells to promote intracellular delivery and ultimately combat intracellular pathogens, with

an emphasis on *Mycobacterium tuberculosis* as an infection model. In more detail, this work is aimed at the following points:

- The study of amphiphilic graft and block copolymers' self-association behavior.
- The using of advanced instrumental methods for the nanostructure and biorelevant properties study.
- Analysis of cytotoxicity and interaction with biological systems.
- The identification and quantification of differences in toxicity, uptake and fate of a nanobead-based intervention.
- Analysis, using several instrumental tools, of the behavior of a selected NP-encapsulated drug and its free form both *in vitro* and *in vivo*.
- The combination of several different approaches/methods ranging from analytical tools and bioanalytical assays to histopathological examinations to critically discuss the chosen nanoformulation properties.

Acknowledgments

This thesis is the culmination of my research over the past 4 years. The work presented and discussed, however, was not done alone. During the abovementioned period, I have been fortunate and thankful to have family, friends, collaborators, mentors, and fellow labmates.

I would like to express my gratitude to my supervisor Mgr. Martin Hrubý, Ph.D., DSc., and advisor prof. RNDr. Pavel Coufal, Ph.D. Martin trusted the naïve and inexperienced me and gave me the opportunity to work on my projects completely independently. I feel thankful for him and for RNDr. Petr Štěpánek, DrSc., advising me through the years spent in the Department of Supramolecular Polymer Systems.

In addition, I would like to thank my colleagues from the IMC CAS for their insightful comments, encouragement, kind help with my research, and analytical and technical services. My sincere thanks go to (alphabetically, without academic degrees): Rafał Konefał, Barbora Koutníková, Miloš Netopilík, Ewa Pavlova, and Tomáš Urbánek.

This work would not have been possible if not for the support of our collaborators; my sincere thanks go to Oto Pavliš, Alejandro Sosnik, Olga Šebestová Janoušková, and Jia-You Fang, who provided me an opportunity to join their team as an intern and/or provided access to their laboratory and research facilities. Additionally, I thank my friends and colleagues in the following institutions/departments: Center of Biological Defense (Military Health Institute, Military Medical Agency, Těchonín, Czech Republic), Laboratory of Pharmaceutical Nanomaterials Science (Department of Materials Science and Engineering, Technion-Israel Institute of Technology, Haifa, Israel), Department of Biological Models (IMC CAS), and Pharmaceutics Laboratory (Graduate Institute of Natural Products, Chang Gung University, Taoyuan, Taiwan). Thanks also go to my external colleagues/coauthors who participated in my research projects and helped me through my study (alphabetically, without academic degrees): Dušan Cmarko, Federico Fenaroli, Gareth Wyn Griffiths, Hen Moshe Halamish, Kenneth Dahl Knudsen, Pavla Kubíčková, Jana Matějková, Ivan Raška, Inbar Schlachet, Zdeňka Syrová and Vít Ulmann.

Note that the results presented in this work reflect just one aspect of a much larger effort. More importantly, I believe that every encounter I have had with my mentors and teachers from previous studies, even the smallest one, has played a significant role in progressing to where I am today. Hence, my thanks go to Miloš Mucala, Blanka Tupá, and Miroslava Zámostná.

Last but not least, the greatest thanks belong to my family and friends for supporting me spiritually throughout my studies and writing of this thesis and my life in general.

Content Endnote

This thesis presents commented research performed over the past 4 years. The first section of the thesis is dedicated to a brief and outlined theoretical background related to infectious diseases and nanobead-based interventions. Note that the multidisciplinary character of the thesis limits the scope of the theoretical part to the main aspects related to the merging field of antibacterial nanomedicines only rather than an exhaustive review. Subsequent sections of the thesis represent a commented overview of the main results obtained according to the specific aims of this work (see above). The materials and methods are described/discussed in detail within each of the publications discussed and attached. The thesis itself, thus, does not contain such content.

My own results-related references used within this work are distinguished from the others using the letter P; for example, [**P5**]. All these papers are attached at the end of this work and are listed in the order in which they are discussed below. Common references and bibliography follow a standard style, for example[17].

In this thesis, dozens of abbreviations are used. For a better orientation, note that an abbreviation written in bold represents a specific formulation/sample characterized, analyzed and/or administered (*e.g.*, The **NPs** have been injected at a dose of 10 mg/kg.). In contrast, abbreviations written as a regular text represent abbreviated text in general, for example, nanoparticles (NPs).

Funding

Financial support from the Czech Science Foundation (grant No. 19-01602S) is acknowledged.

LIST OF SYMBOLS AND ABBREVIATIONS

Symbols

$Đ$	Dispersity
D_g	Diameter of gyration (nm)
D_h	Hydrodynamic diameter (nm)
M_w	Weight average molecular weight (Da)
M_n	Number average molecular weight (Da)
IC50	Half maximal inhibitory concentration (μg/mL)
AUC	Area under the concentration–time curve
C_{max}	Maximum concentration in serum or lung tissue (μg/mL or μg/g, respectively)
T_{max}	Time to maximum concentration (h)
$T_{1/2}$	Elimination half-life (h)

Abbreviations

^{1}H NMR	Proton nuclear magnetic resonance
AFFFF	Asymmetric flow field flow fractionation
BA	Boric acid
BCG	Bacillus Calmette–Guérin
CAN	Cerium ammonium nitrate
CFU	Colony-forming unit
CS	Chitosan
DACCA	7-(Diethyl amino)coumarin-3-carbonyl azide
DC	Dendritic cell
DIC	Differential interference contrast
DL	Drug loading
DLS	Dynamic light scattering
EE	Entrapment efficiency
EPR	Enhanced permeability and retention
FDA	Food and Drug Administration
FFF	Field-flow fractionation
FSC	Forward scatter

GPC	Gel permeation chromatography
H&E	Hematoxylin and eosin stain
HIV	Human immunodeficiency virus
i. p.	Intraperitoneally
IMC CAS	Institute of Macromolecular Chemistry, Czech Academy of Sciences
MDR	Multidrug resistance
MIC	Minimum inhibitory concentration
MPEO	Methoxy poly(ethylene oxide)
MPS	Mononuclear phagocyte system
MTT	Methylthiazolyldiphenyl-tetrazolium bromide
NP	Nanoparticle
P4HB	Poly(γ-butyrolactone)
PCL	Poly(ε-caprolactone)
PEO	Poly(ethylene oxide)
PGA	Poly(γ-glutamic acid)
PHPMA	Poly[N-(2-hydroxypropyl)methacrylamide]
PLA	Poly(D,L-lactic acid)
PLGA	Poly(D,L-lactic-*co*-glycolic acid)
PMMA	Poly(methyl methacrylate)
PMOX	Poly(2-methyl oxazoline)
PVA	Poly(vinyl alcohol)
QELS	Quasi-elastic light scattering
RIF	Rifampicin
SANS	Small-angle neutron scattering
SLS	Static light scattering
SSC	Side scatter
TB	Tuberculosis
TEM	Transmission electron microscopy
TEMED	Tetramethylethylenediamine
TMR	Tetramethylrhodamine-5-carbonyl azide
TPP	Tripolyphosphate
UV/VIS	Ultraviolet–visible spectroscopy
WHO	World Health Organization
XDR	Extensive drug resistance
ZN	Ziehl–Neelsen staining

CHAPER 1: THEORETICAL PART

1.1 Intracellular Infections

1.1.1 Bacteria Actively Invade Host Cells

One of the essential aims of living systems is to colonize all the environment available. To date, more than 200 prokaryotic bacteria have been reported to be able to infect human hosts and cause disease. For example, some bacterial pathogens colonize the gastrointestinal (*e.g.*, enteropathogenic and enterotoxigenic *Escherichia coli*) or urogenital (*e.g.*, *Neisseria gonorrhoeae*) tract, skin, or oral mucosa (*Streptococcus* spp.). Some pathogens actively enter host cells, resist the intracellular environment (*e.g.*, cytosol and phagosome) and replicate (*e.g.*, *Legionella pneumophila*). Given this background, pathogenic bacteria can be categorized into extracellular, facultative intracellular, and obligate intracellular pathogens[1,2]. The bacterial entrance to the host cells is determined by complex molecular and cell phenomena whose description, however, exceeds the framework of this thesis. Intracellular bacteria thrive inside professional phagocytes and are one of the most efficient cell types of first-line antimicrobial defense, macrophages and dendritic cells. Alternatively, neutrophils, fibroblasts, or epithelial cells serve as an important habitat for intracellular pathogens[3].

Intracellular bacteria-caused diseases (*e.g.*, tuberculosis, legionellosis, and tularemia) are hard to treat. Several bacterial strains are able to produce a "silent" intracellular infection and, thus, escape from the host cells' bactericidal mechanisms. These infected cells are not only unable to kill the intracellular milieu-presenting pathogen but also may act as niches and allow the spread of the infection to other cells. Similarly, their intracellular location allows for protection of such invading bacteria; they are protected from the immune system as well as from conventional treatment[4]. This is due to the inability of conventional antibacterial agents to penetrate the cell membrane. Hence, these infections represent a major cause of global morbidity and mortality.

The bacterial intracellular pathogen *M. tuberculosis*, the etiologic agent of tuberculosis, is the selected infection model for this thesis.

1.1.2 Tuberculosis

Tuberculosis is an infectious disease caused by *M. tuberculosis*, a slender, nonmotile and acid-fast bacillus. Mycobacteria possess a waxy coating on the surface of their cell wall that is composed mainly of mycolic acids. Therefore, *M. tuberculosis* is resistant to dehydration, has low permeability to hydrophobic antibiotics and has a high survivability[5].

TB is primarily transmitted via the inhalation route, and the main site of infection is the lungs (**Fig. 1.1**). Innate cell-mediated immunity and alveolar macrophages that interact with the invading pathogen represent the first line of cellular defense. Macrophages are unable to kill the deposited mycobacteria, which continue to replicate until overgrowing and disseminating from ruptured host cells, after which an adaptive immune response occurs. Dendritic cells (DCs) can also play a crucial role in host defense by presenting antigens and activating both T and B cells[6]. Subsequently, granulomas are formed. In most cases, this promotes nonsterile control of the pathogen. The majority of infected individuals will remain in a stable asymptomatic stage called latent TB, while in hosts with efficient cell-mediated immunity, the infection may be eradicated permanently. Subsequently, healed granulomas leave small calcified lesions. Progressive TB will eventually occur in a small percentage of infected individuals. In this case, the hallmark of reactivation is the failure of the host immune

response. As depicted in **Fig. 1.1**, the exacerbation of necrotic cell death then leads to extensive caseous lesions; rupture of the granulomas into the airways occurs. Given this, people who have an active TB infection can then generate infectious aerosols by coughing[7,8].

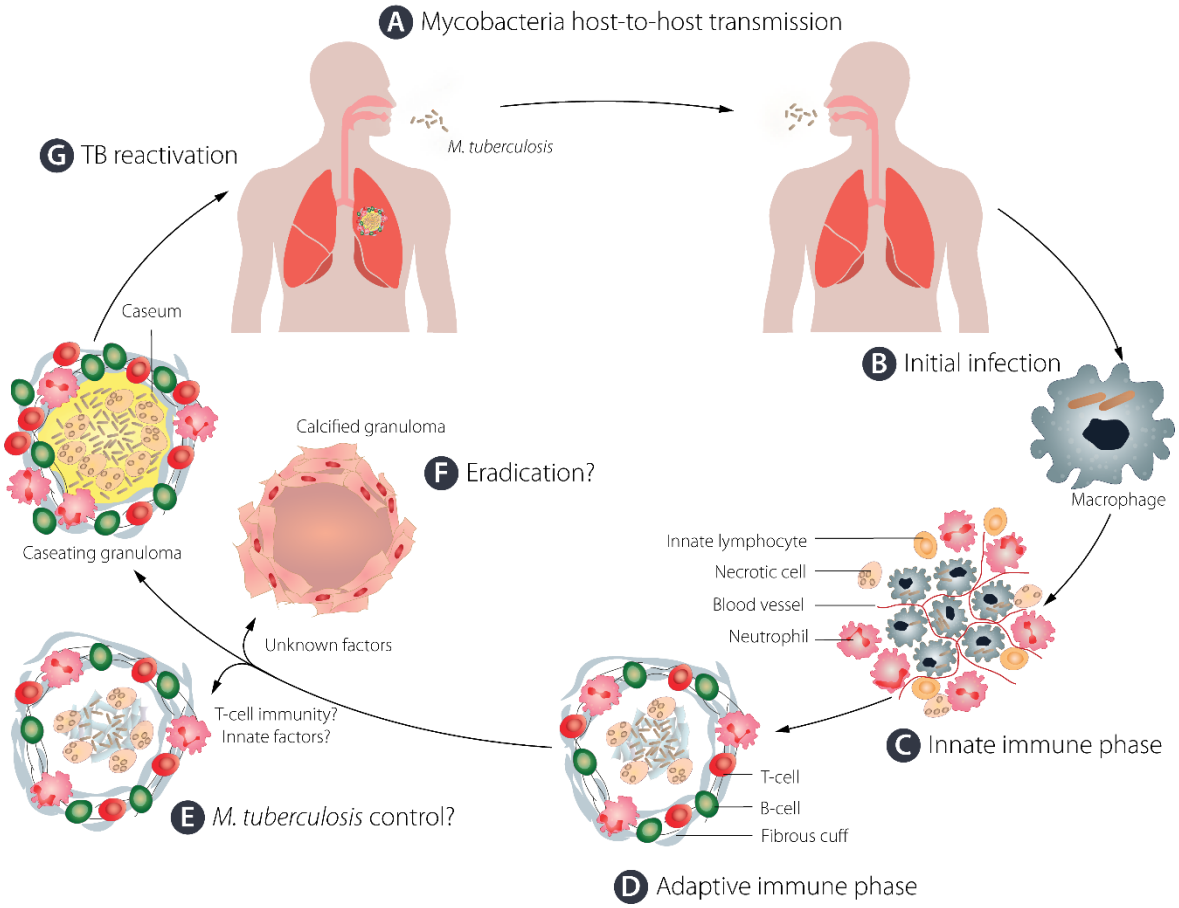

Figure 1.1 TB pathogenesis. Infection is transmitted by inhalation of expelled bacteria (**A**). The defense mechanisms involve an innate immune response (**B**) and an adaptive immune response (**C**) based on the recruitment of T-cells, B-cells and other leukocytes. Granulomas are formed due to this immune response; nonsterile control of mycobacteria (**E**) is promoted in most cases. The majority of patients will remain in latent tuberculosis. TB may be eradicated permanently in patients with efficient cell-mediated immunity (**F**). Active TB will eventually occur in 5–15% of previously infected hosts (**G**). Adapted from reference[9].

TB treatment is very complicated and must be carried out using a cocktail of antibiotics. Usually, the preferred regimen consists of an intensive phase of first-line anti-TB drugs (isoniazid, rifampicin, pyrazinamide and ethambutol) followed by a 4-month continuation phase of isoniazid and rifampicin. Note that although potentially curative interventions have been available for approximately 50 years, TB remains the leading cause of preventable death in the world[10,11].

The main causes of failure and relapses in conventional therapies and TB eradication are the high resistance of mycobacteria, the inability to detect all stages of TB, inadequate medical care in most of the world, and poor patient compliance[12-14]. Finally, two additional complications of the therapy are the selection of *M. tuberculosis* strains that possess multidrug resistance (MDR, defined as resistance to both rifampicin and isoniazid) and extensive drug resistance (XDR, defined as resistance to at least one second-line injectable drug and any fluoroquinolone drug) and the increase in the number of TB-affected patients who are coinfected with HIV.[11]

Given these factors, improved strategies are needed to shorten the TB treatment duration and avoid selection of drug-resistant mutants. The three main strategies that are worth attention lie in the development of novel drugs[15], vaccination improvement[16], and drug delivery systems based on nanomedicines[11].

1.2 Introducing Polymeric Nanobeads

A drug can be delivered into an infected cell by several different kinds of submicron vehicles. These include lipid systems such as liposomes[17], inorganic NPs such as gold and iron oxide NPs[18], carbon nanotubes[19], silica nanobeads[20], *etc*. The scope of this work is, however, limited to polymeric NPs only, as polymers are the most common materials for constructing NP-based carriers[21].

In this context, amphiphilic polymer NPs are known as emerging devices allowing solubilization, stabilization, and delivery of various chemotherapeutics. The functional properties of amphiphilic polymer NPs render them ideal and unique. The amphiphilic NP matrix of amphiphilic copolymers consists of at least two regions possessing distinct chemical natures. This structure results in phase separation into supramolecular architectures, often having diameters in the nanometer range, as a result of chain association, a phenomenon known as self-assembly. During this process, the hydrophobic regions assemble to form the core region. The hydrophilic regions, in contrast, form the layer between the core and the external aqueous environment, colloidally stabilize the NPs in an aqueous milieu and often extend the blood-circulation time while reducing uptake by phagocytes, phenomena known as stealth properties (see below). Both the hydrophilic and hydrophobic regions are capable of entrapping and delivering a wide range of both polar and nonpolar drugs[22, 23]. Amphiphilic copolymers can be of alternating[24], block[25], random[26], graft[27], star[28], or brush[29] type architectures (**Fig. 1.2**). The simplest structure is the random copolymer. The use of random copolymers is, however, complicated due to the low reproducibility of such systems. Thus, block and graft copolymers, for example, generate more significant interest[23].

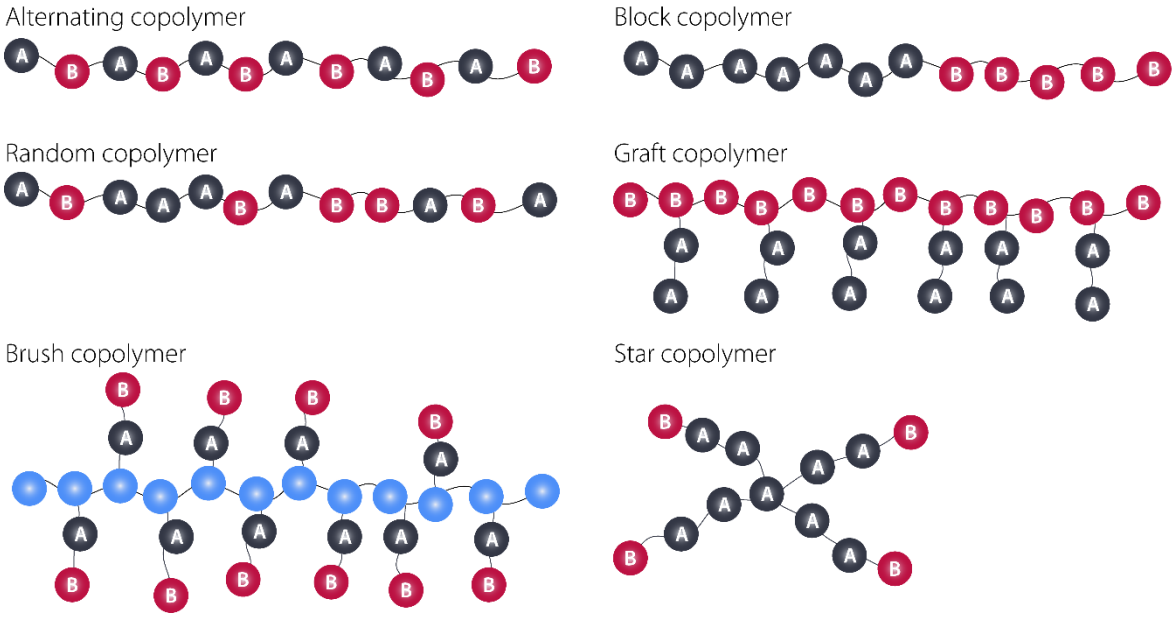

Figure 1.2 Different forms of copolymers

There are a variety of both hydrophobic and hydrophilic monomers used in the fabrication of amphiphilic copolymers, with some of the common examples listed in **Table 1.1**. Hydrophilic

polymers, as suggested above, stabilize the hydrophobic region of NPs by way of hydrophilic-hydrophobic balance control; some common examples are poly(ethylene oxide) (PEO), poly(2-methyl oxazoline) (PMOX), and poly[N-(2-hydroxypropyl)methacrylamide] (PHPMA). Similarly, water-soluble polysaccharides—natural carbohydrate derivatives containing chains of mono-saccharide subunits—have been widely used by humans, as they are considered to be superior to other polymers due to their ease in tailoring, biocompatibility, and bioactivity[30].

Importantly, due to changing the NP surface energy, hydrophilic polymers can exhibit a "stealth" property. As mentioned below, one of the significant obstacles to the long-term circulation of drug delivery interventions is clearance by the mononuclear phagocyte system (MPS)[31] (see below).

Table 1.1 Representation of some of the common hydrophilic and hydrophobic polymers

Hydrophilic	Hydrophobic
Poly(ethylene oxide) PEO 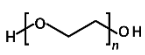	**Poly(ε-caprolactone)** PCL 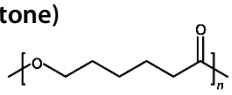
Poly(2-methyl oxazoline) PMOX 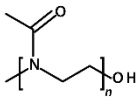	**Poly(γ-glutamic acid)** PGA 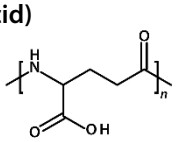
Poly(vinyl alcohol) PVA 	**Poly(D,L-lactic acid)** PLA 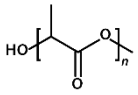
Poly[N-(2-hydroxypropyl)methacrylamide] PHPMA 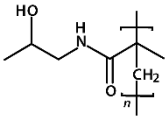	**Poly(D,L-lactic-*co*-glycolic acid)** PLGA 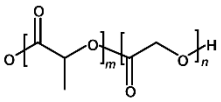
Poly(ethylene imine) PEI 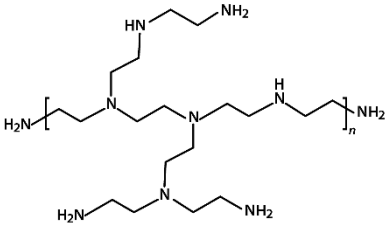	**Poly(methyl methacrylate)** PMMA 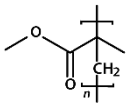

A typical example of a hydrophobic polymer is poly(methyl methacrylate) (PMMA), which is one of the most widely explored biomedical materials due to its biocompatibility[32]; biocompatibility is a property by which a material does not produce a toxic or immunological response in a biological environment. PMMA is, however, nonbiodegradable. Biodegradable polymers are more useful for biomedicine. For example, enzymatically and hydrolytically degradable poly(D,L-lactic acid) (PLA), poly(D,L-lactic-*co*-glycolic acid) (PLGA), and poly(ε-caprolactone) (PCL) are widely used for the fabrication of biocompatible and fully or partially degradable carriers[33].

1.2.1 There Are a Variety of Polymeric NP Preparation Methods

Once the amphiphilic copolymer has been synthesized, it can then be assembled into a supramolecular drug delivery system using a number of different techniques[23]. A typical approach based on emulsification includes two steps—preparation of an emulsified system and subsequent NP formation. Most of these preparation methods are based on mechanical processes homogenizing two immiscible phases in the presence of a surface-active agent[34]. A typical example is PLGA NPs; PLGA is dissolved in a water-immiscible or partially water-miscible solvent (*e.g.*, dichloromethane, chloroform, and ethyl acetate) and added to an aqueous surfactant solution (*e.g.*, PVA). Subsequently, exposure to a high-energy source, such as an ultrasonic device, and solvent evaporation are carried out[34].

A second typical approach does not require the preparation of an emulsion. One of the easiest preparation methods, called the solvent displacement method, is based on the nanoprecipitation of a polymer. Three basic components—the polymer, the polymer solvent, and the polymer nonsolvent—are typically used. To produce the assemblies, the polymer solution (*e.g.*, in acetone) is added to an aqueous medium. The organic solvent is then displaced, for example, by evaporation. Because of the self-assembly behavior of macromolecules, this results in spontaneous formation of NPs. Note that a significant part of the polymeric systems prepared *via* nanoprecipitation is based on block copolymers, as these polymers exhibit amphiphilic character[35]. Nanoprecipitation can, however, also be used in the case of nonamphiphilic, purely hydrophobic polymers such as PLA and PCL; in such cases, the presence of detergent in the aqueous phase is often required. In addition to the two techniques outlined above, there are a variety of other methods, including salting out, dialysis, and spray drying[36].

An active cargo can be embedded in the particle matrix either by covalent bonding or by drug entrapment[37]. In the first case, the synthesis of polymeric conjugates with a drug is required. These drug conjugates are then used for NP fabrication, as suggested above. Note that the covalent approach generally requires chemical modification that can affect the efficiency. Moreover, this approach leads to a new molecule, making the potential clinical approval process more complicated. The second approach has the ability to employ active drugs — a hydrophobic drug can be embedded within the excipient-like NP matrix because hydrophobic drugs have an affinity for the hydrophobic core of a nanobead[38].

1.3 Brief Overview into Characterization and Biorelevant Analysis

To achieve the suggested advantages offered by nanomedicines and test them *in vivo* or within clinical studies, challenges such as developing nontoxic systems, achieving and improving biocompatibility, realizing effective drug loading, attaining efficient targeting, and achieving transport and release ability must be considered[39]. Thus, once a nanobead-based formulation is prepared, there is a need for robust and detailed study of all the relevant properties. Physicochemical characterization[40] is aimed at the study of properties such as nanobead size, size distribution, charge, and morphology. As evident from the attached publications, two of the key techniques are light scattering methods: dynamic light scattering (DLS) and static light scattering (SLS)[41]. No less important is the study of the interaction with biological systems *in vitro*. A comprehensive theoretical description of all the relevant methods is not, however, possible. Thus, let the attached publications be an example of experimental methods and emphasize this emerging area of biorelevant analysis of nanomedicines. Below, some chosen methods are described in more detail.

1.3.1 Dynamic Light Scattering

To study nanobead size and size distribution, DLS is an elegant tool. This nondestructive method, also known as quasi-elastic light scattering (QELS), is based on the measurement of scattered light intensity fluctuations. In a DLS experiment (**Fig. 1.3A**), a single-frequency laser is directed onto the inspected sample. The incident laser light is scattered in all directions when particles are present in the sample. At a certain angle, the scattered light intensity is detected over time. Brownian motion of the particles causes a Doppler shift in the frequency of the incident light; this change in light frequency cannot, however, be detected spectroscopically. One can observe the light intensity fluctuations caused by Brownian motion of the particles that are present. Logically, smaller entities, which move faster, undergo faster fluctuations than larger entities[42]. Thus, the particle mobility can be analyzed using the intensity autocorrelation function $g(t)$, which, for a monodisperse system, is given by:

$$g(t)=1+\beta(e^{-\Gamma t})^2 , \tag{1}$$

where β is an instrumental constant and Γ is the relaxation frequency, defined by the relaxation time τ and the diffusion coefficient D of the particle:

$$\Gamma=\frac{1}{\tau}=Dq^2 , \tag{2}$$

where q is the absolute value of the scattering vector that is defined using the wavelength λ, the refractive index of the solvent n and the scattering angle θ:

$$q=\frac{4\pi n}{\lambda}\sin(\theta/2) . \tag{3}$$

Using the diffusion coefficient, the particle size can be calculated by the Stokes–Einstein equation as the hydrodynamic diameter D_H.

$$D=\frac{k_B T}{3\pi\eta D_H} , \tag{4}$$

where k_B is the Boltzmann constant, T is the absolute temperature, and η is the dynamic viscosity of the solvent.

1.3.2 Static Light Scattering

Another scattering method for the study of nanobead size is SLS (the instrumental scheme is depicted in **Fig. 1.3A**). This method evaluates the scattered light intensity as a function of the scattered light detector angle. Average intensity values over certain time periods are considered[43]. The classical theory, which considers the wavelength λ to be significantly higher than the particle radius r, was formulated by Rayleigh. Given the practical aspects of an SLS experiment, the Zimm equation should be stressed:

$$\frac{Kc}{R}=\frac{1}{M_w^{NPs}}\left(1+\frac{1}{3}R_G{}^2q^2\right)+2A_2c , \tag{5}$$

where K refers to the optical constant, R is the Rayleigh ratio, c is the concentration, M_w^{NPs} is the particle molecular weight, R_G is the radius of gyration, q is the scattering vector (see Eq. 3), and A_2 is the second virial coefficient. The constant K can be described by the following formula:

$$K = \frac{4\pi^2 n_{std}^2 (dn/dc)^2}{N_A \lambda^4}, \quad (6)$$

where n_{std} is the refractive index of the scattering standard (usually toluene), N_A is the Avogadro constant, and dn/dc is the refractive index increment.

When the Zimm diagram is constructed (**Fig. 1.3B**), zero angle and zero concentration extrapolations are obtained; the reciprocal molecular weight can be expressed as the inverse vertical axis intercept. Additionally, using the zero angle and zero concentration extrapolation slopes, both A_2 and R_G can be expressed. Note that A_2 reflects the energy of interactions between the solvent and the particles: when $A_2 > 0$, the solvent is "good", and the particulate formulation tends to be stable; when $A_2 < 0$, the solvent is "poor", and the particulate formulation tends to form aggregates. When A_2 equals 0, the solvent can be described as a theta solvent.

In contrast to DLS, which is sensitive mainly to dynamic processes (*e.g.*, mobility of particles), SLS can be used for the study of the molecular weight, the particle structure, and the particle interaction with the solvent used. Importantly, when DLS and SLS analyses are combined, the D_G/D_H ratio, where D_G is the diameter of gyration, provides significant information on the architecture. In other words, it can be used for the estimation of particle deviation from the shape of a homogeneous sphere that possesses a ratio of 0.775[44].

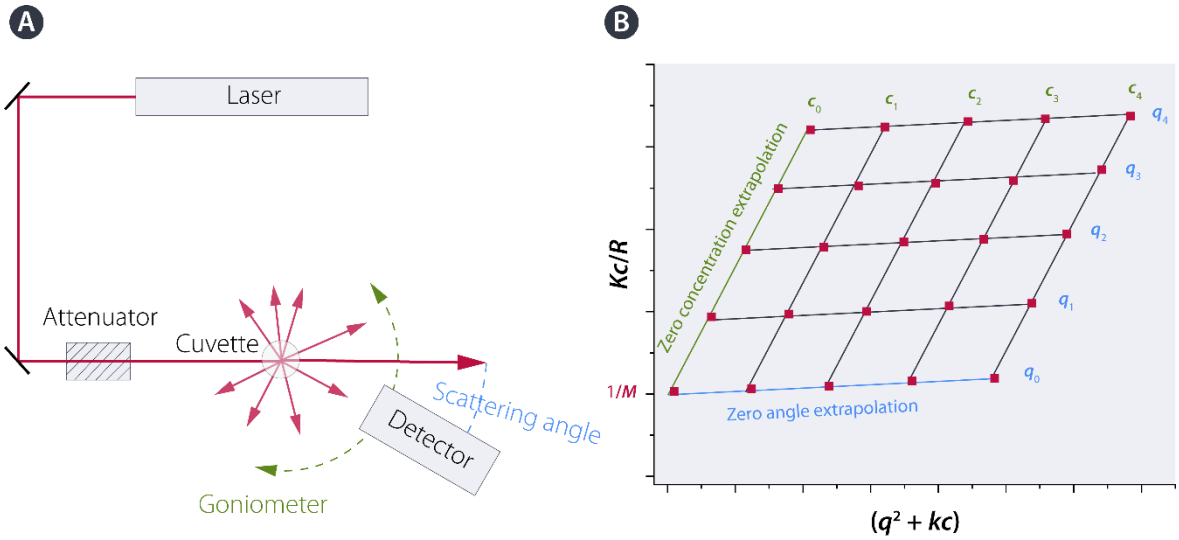

Figure 1.3 Light scattering methods are essential tools for the analysis of nanobeads. (**A**) The instrumental scheme is depicted. In a DLS experiment, a single-frequency laser is directed onto the dispersion of nanobeads. The incident laser light is scattered in all directions. At a certain angle, the scattered light is detected over time as scattered light fluctuations. In an SLS experiment, the same instrument allows measuring at several different angles; the absolute mean intensity is measured. (**B**) Static light scattering experimental data processing. One can plot Kc/R as a function of $(q^2 + kc)$, where k is an arbitrary constant.

1.3.3 Asymmetric Flow Field Flow Fractionation

As evident from the attached publication, complementary analytical tools were combined to assess NP properties. For example, asymmetric flow field flow fractionation (AFFFF) can be applied to the characterization of nanoparticles, polymers and proteins. It is a chromatographic elution technique in the versatile field-flow fractionation (FFF) separation tool family. FFF was first described by J. C. Giddings in 1976[45]. Similar to chromatography, typical FFF experiments involve the introduction of

a narrow sample band into a mobile phase stream flowing through a channel where separation occurs (**Fig. 1.4A**). The laminar flow of the mobile phase is generally described by a parabolic flow profile, in which the stream velocity varies with the distance from the channel walls. Zero velocity flow can be observed at the walls, while the flow increases farther away from the wall. The maximum velocity can be observed at the center of the channel. In this technique, retention/separation is achieved by way of the nonuniform flow profile in the mobile phase with a force field (*e.g.*, gravitational, thermal-gradient, electrical, and magnetic) introduced at a right angle to the channel. The entities analyzed migrate at different speeds, as different entities are held by the field in different regions. The separation is hence due to the combined effect of the applied field and the mobile phase flow velocity profile and is determined by the differences in the diffusion coefficients of the entities. Eluted species are then detected (e.g., by a UV/VIS detector)[46].

In AFFFF, the bottom channel wall is replaced with a semipermeable membrane (regenerated cellulose) with a defined cutoff size, allowing both the mobile phase and small entities below the cutoff to penetrate the membrane[47]. In this technique, cross-flow is the force leading to sample accumulation, as depicted in **Fig. 1.4B**. A typical AFFFF experiment starts with sample injection and a focusing step in which two flows in opposite directions are applied to the channel. This focuses all the entities in the sample to one area and corrects for any peak broadening. Next is the elution step (**Fig. 1.4C**) in which a single-direction solvent is introduced. Small entities with high diffusion coefficients are eluted at an early time point. Large particles with low diffusion coefficients are eluted later. In the field of macromolecular analytes, AFFFF is usually coupled with refractive index (RI), UV/VIS, and multiangle light scattering (MALS) detectors that are based on the light scattering phenomenon outlined above. Due to the separation process, MALS detection allows estimation of both D_G and M_w values, even when polydisperse samples are analyzed. This is probably the largest advantage compared to conventional DLS, which is usually biased due to the presence of larger particles.

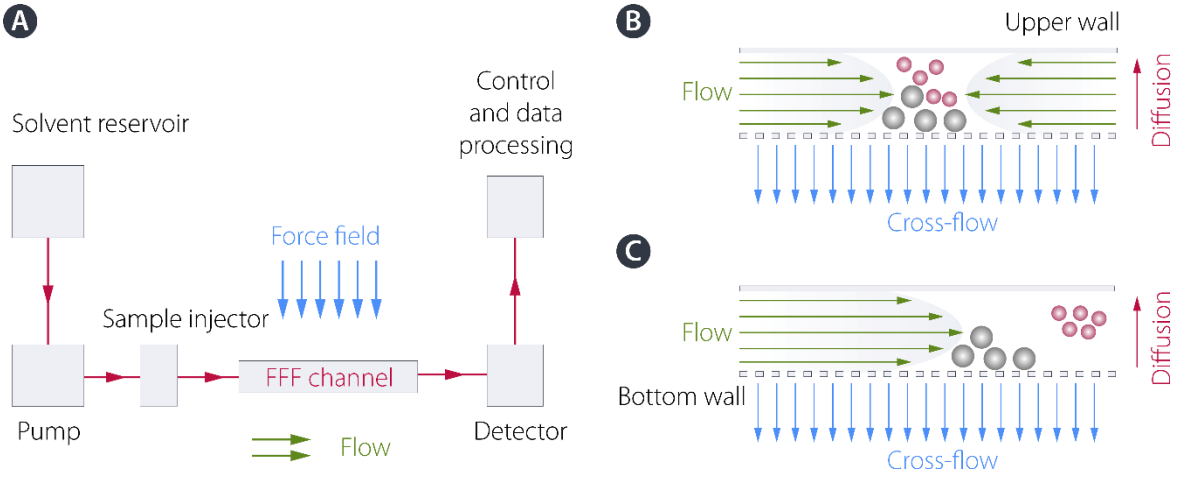

Figure 1.4 Asymmetric Flow Field Flow Fractionation. (**A**) FFF instrumental setup. A typical AFFF experiment starts with an injection/focusing step (**B**) followed by separation (**C**).

1.3.4 NP interaction with Cells

In the context of nanoparticle drug delivery systems, it is not surprising that the use of such interventions bears a risk of side effects. Thus, the use of *in vitro* biological models in conjunction with bioanalytical tools vastly improves the understanding of the predictability and potential effects *in vivo* before clinical trials.

As the author of this thesis finds, there are two major quests. The first question to be answered—*How does a cell process nanobead-based interventions?*—refers to the movement of nanomedicines through a cell (**Fig. 1.5**). This area is aimed at the study of NP uptake, mechanisms of internalization (see below), NP fate, *etc*. One of the most usable bioanalytical and biological tools assessing these phenomena is the use of fluorescently labeled NPs[48]. Additionally, as evident from the attached publications, methods such as confocal microscopy and flow cytometry are essential instrumental methods that are extremely applicable in this area[49].

In contrast, the second question—*What is the cell's biological response?*—takes into account the complex interactions between the nanomedicines and the cell. Two types of cell-based assays studying the effects of NPs can be classified—functional and viability assays[50]. Functional assays are primarily aimed at determining the impacts of nanobeads on cell function and pathways. These assays include, for example, the study of cell proliferation (*i.e.*, growth), oxidative stress, immunogenicity by way of cytokine determination, and the impact on both DNA synthesis/damage and gene expression. Viability assays are primarily focused on whether cells in the assay remain viable after nanobeads have been added to the culture. These include the study of hemolytic activity (*i.e.*, the impact on red blood cells) and cytotoxicity described in more detail below.

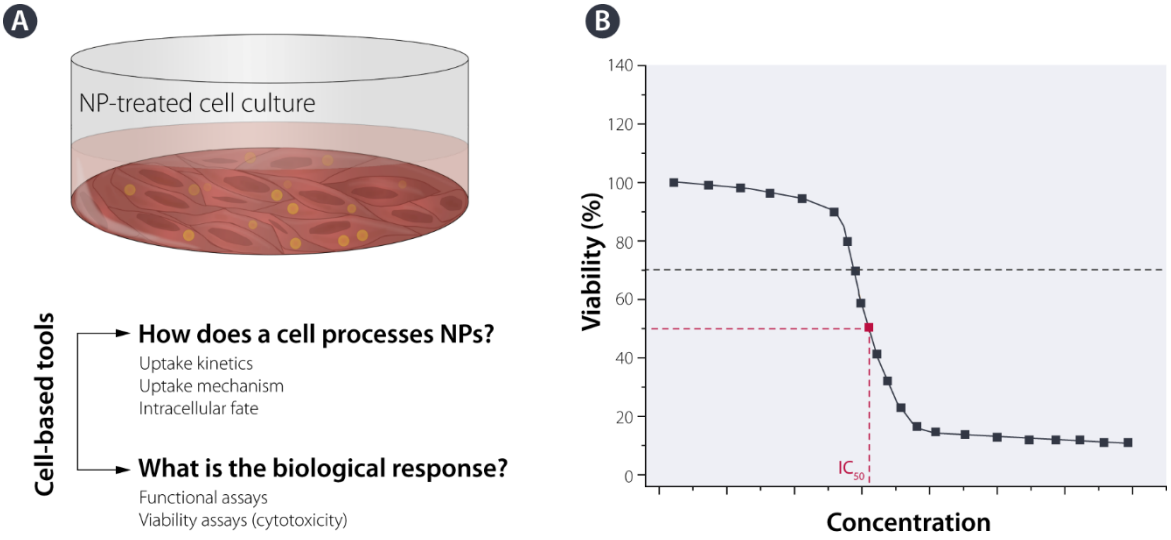

Figure 1.5 Biorelevant analysis of nanobead-cell interactions. (**A**) There are two main quests to be assessed in terms of a general cell culture experiment depicted above left. (**B**) A typical result from the cytotoxicity assay. The horizontal line in the panel indicates a cell viability level where the data above the line are considered noncytotoxic and those below the line are cytotoxic. The half maximal inhibitory concentration (IC_{50}) can be used as a quantitative value related to cytotoxicity.

1.3.5 Cytotoxicity assays

Since Kawahara used a cell culture method to study dental material cytotoxicity in 1955[51], a variety of cytotoxicity assays have been adapted. Cytotoxicity assays determine cell viability, *i.e.*, the percent of healthy cells in nanobead-treated cells usually after 24 h of incubation. One of the simplest assays is dye exclusion. This approach uses membrane-impermeable dyes that stain only cells with damaged cell membranes. Dyes such as trypan blue, 7-amino-actinomycin D, and propidium iodide are selective stains for dead cells in this way. Determination of the dye used is based on fluorescence or absorbance measurements. Another example is the measurement of cell metabolic activity—after 24 h of cell treatment, a dye is added to the culture. If the cells are viable, the dye is reduced to

a colored or fluorescent product. Cytotoxicity assays are usually carried out with cells with desired characteristics (*e.g.*, epithelial, endothelial, and fibroblasts) and performed within 96-well microtiter polystyrene plates. These *in vitro* experiments can be evaluated according to ISO 10993-5; reduction of cell viability by more than 30% is considered a cytotoxic effect[52] (**Fig. 1.5B**).

1.3.6 Flow Cytometry

A powerful method capable of addressing both of the abovementioned issues (*i.e.*, cells' impact on NPs and NPs' impact on cells) is flow cytometry. It is a bioanalytical tool that assesses multiple features of a single cell, such as size, granularity, and fluorescence, simultaneously as a cell suspension flows through a measuring device. Herein, the general principle is explained.

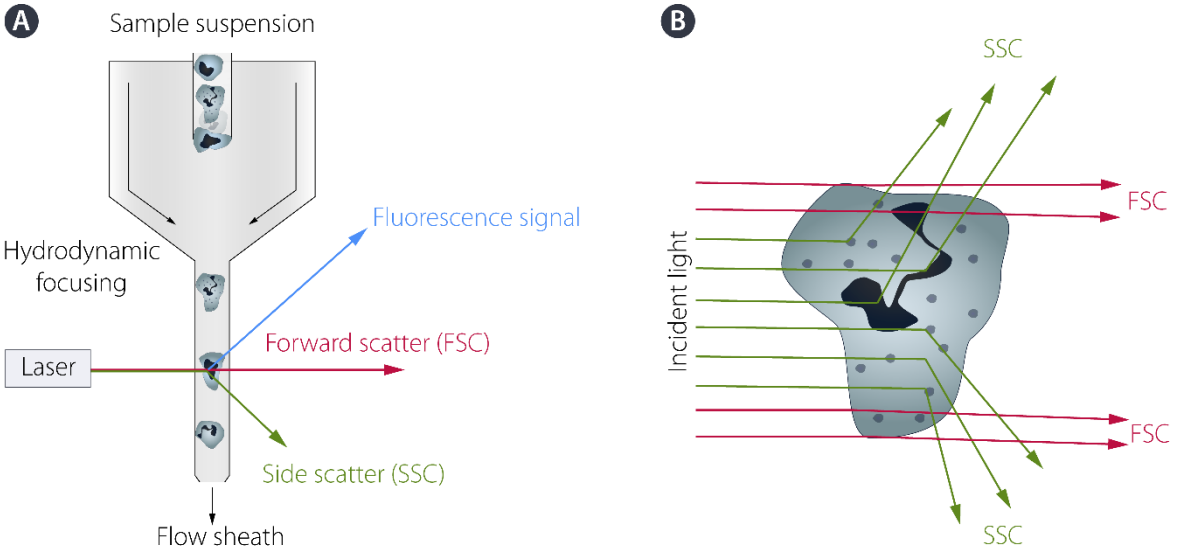

Figure 1.6 Flow cytometry as a cell-analyzing bioanalytical tool. (**A**) As scheme of the nonsorting flow cytometer is shown. (**B**) Illustration of light scattering by a cell. Forward scatter (FSC) is proportional to size and surface area, while side scatter (SSC) is proportional to cell granularity.

The first essential component of a flow cytometer (**Fig. 1.6A**) is the fluidic system consisting of sheath fluid and pressurized lines that inject both the sheath fluid and the suspended cells into the flow chamber. Based on principles related to laminar flow, the analyzed suspension core remains separate though coaxial within the sheath buffer, while the sheath buffer accelerates the cells and restricts them to the sample core, a phenomenon known as hydrodynamic focusing, making the cells align in a single file fashion. In fixed positions, the flow cytometer has a laser, lenses, and collection optics. Interactions between the cells and a laser light beam are measured as light scattering and/or fluorescence intensity.

Upon light scattering, the light is deflected around the edges of the cell analyzed after the laser strikes the cells; one detector is in line with the light beam, and the second detector is placed perpendicular to the stream. Importantly, two types of light scatter, forward scatter (FSC) and side scatter (SSC), are detected (**Fig. 1.6B**). While FSC light is proportional to cell surface area or size, SSC light represents mostly refracted and reflected light and is proportional to the cell granularity and complexity, allowing cell immunophenotyping, for instance[53, 54].

Flow cytometry is, however, predominantly used to measure the fluorescence intensity of fluorescent dyes, antibodies, or ligands binding to specific cell-associated molecules[55]. For instance, this allows

the measurement of apoptosis markers, cell viability, detection of plasma membrane changes, and DNA fragmentation, *i.e.*, the functional and viability assays suggested above. Importantly, as evident from some of the attached publications, flow cytometry is a powerful tool for the study of nanobead uptake, uptake kinetics and intracellular fate — using fluorescent nanobead subjected to a cell culture, this technique is capable of assessing the cell-associated fluorescence.

Note that two different types of flow cytometry are available, namely, nonsorting and sorting. While nonsorting systems perform light scattering and fluorescence emission only, the sorting systems possess the ability to sort the cells as well.

1.4 Rationalizing the Use of Nanomedicines

NP drug delivery represents a unique and useful approach that has been shown to improve the efficacy while decreasing the doses and off-target toxicities[11, 56, 57]. To rationalize the use of nanomedicines, dozens of factors could be discussed and emphasized. Below, selected intracellular drug delivery-relevant phenomena are mentioned to outline this emerging area.

1.4.1 Nanobeads Reach Intracellular Levels

Logically, to treat an infection caused by bacteria that are capable of living and reproducing within a cell, there is a requirement for intracellular delivery of an active molecule (*i.e.*, an antibiotic). This is satisfied by the fact that, owing to their small size, NPs can easily enter eukaryotic cells such as macrophages and epithelial cells—two important cell types representing niches for bacterial persistence[58-60].

In general, NPs are engulfed by a cell mainly through endocytosis (**Fig. 1.7**), a biologically important process allowing internalization of a material. This process is based on cell membrane invaginations, followed by complex steps. Depending on the cell type and NP properties, endocytosis can be classified into two major categories: phagocytosis (*i.e.*, "cell eating") and pinocytosis (*i.e.*, "cell drinking")[60].

Phagocytosis occurs primarily in the case of professional phagocytes (neutrophils, macrophages, and dendritic cells). Their aim is to take up dead cells, cell debris, and bacterial pathogens, *i.e.*, relatively large structures. Membrane protrusions surround structures to be ingested and absorb them into phagosomes that are formed by the fusion of cell membranes. Integral phagocytosis is a process called opsonization—soluble opsonins (*e.g.*, immunoglobulins and complement proteins) coat the target structures to initiate phagocytotic activity[61]. Opsonins serve as adaptors that bind and activate potent phagocytic receptors. Opsonization, however, also occurs in the case of human-fabricated beads. When exposed to physiological conditions, the nanostructure surface is associated with various biomolecules to decrease the surface energy. This leads to the formation of a layer—the protein corona[62]. Note that this phenomenon has several relevant implications, such as the effect of the protein corona on colloidal stability and rapid clearance by the mononuclear phagocyte system (MPS)[31].

Pinocytosis can be subcategorized into clathrin-mediated endocytosis, caveolae-mediated endocytosis, clathrin- and caveolae-independent endocytosis and macropinocytosis[63]. In clathrin-mediated endocytosis, particular ligands in the extracellular environment bind to the receptors on the surface of the plasma membrane. This leads to the formation of a ligand-receptor complex. These complexes move to a specialized region of the plasma membrane that is rich in clathrin. Subsequently, they are taken up through the formation of clathrin-coated vesicles[64]. Once internalized, clathrin coatings are expelled prior to fusion with early endosomes.

Caveolae-mediated endocytosis represents the route of cell entry that involves flask-shaped invaginations in the plasma membrane called caveolae (little caves). The caveolae are present in endothelial, epithelial, adipocyte, muscle, and fibroblast cells and are composed of the membrane protein caveolin-1. Once caveolae are detached from the plasma membrane, they fuse with caveosomes and vesicular structures. Clathrin- and caveolae-independent endocytosis occurs in cells that are deprived of clathrin and caveolin. Finally, macropinocytosis is a subtype of the pinocytosis mechanism in which cells take in high volumes of extracellular fluid by forming relatively large vesicular structures called macropinosomes. This pathway internalizes apoptotic and necrotic cells, bacteria, and viruses as well as presented antigens. Even certain micron-sized architectures that cannot be taken up by cells by most other pathways can be internalized through macropinocytosis[60].

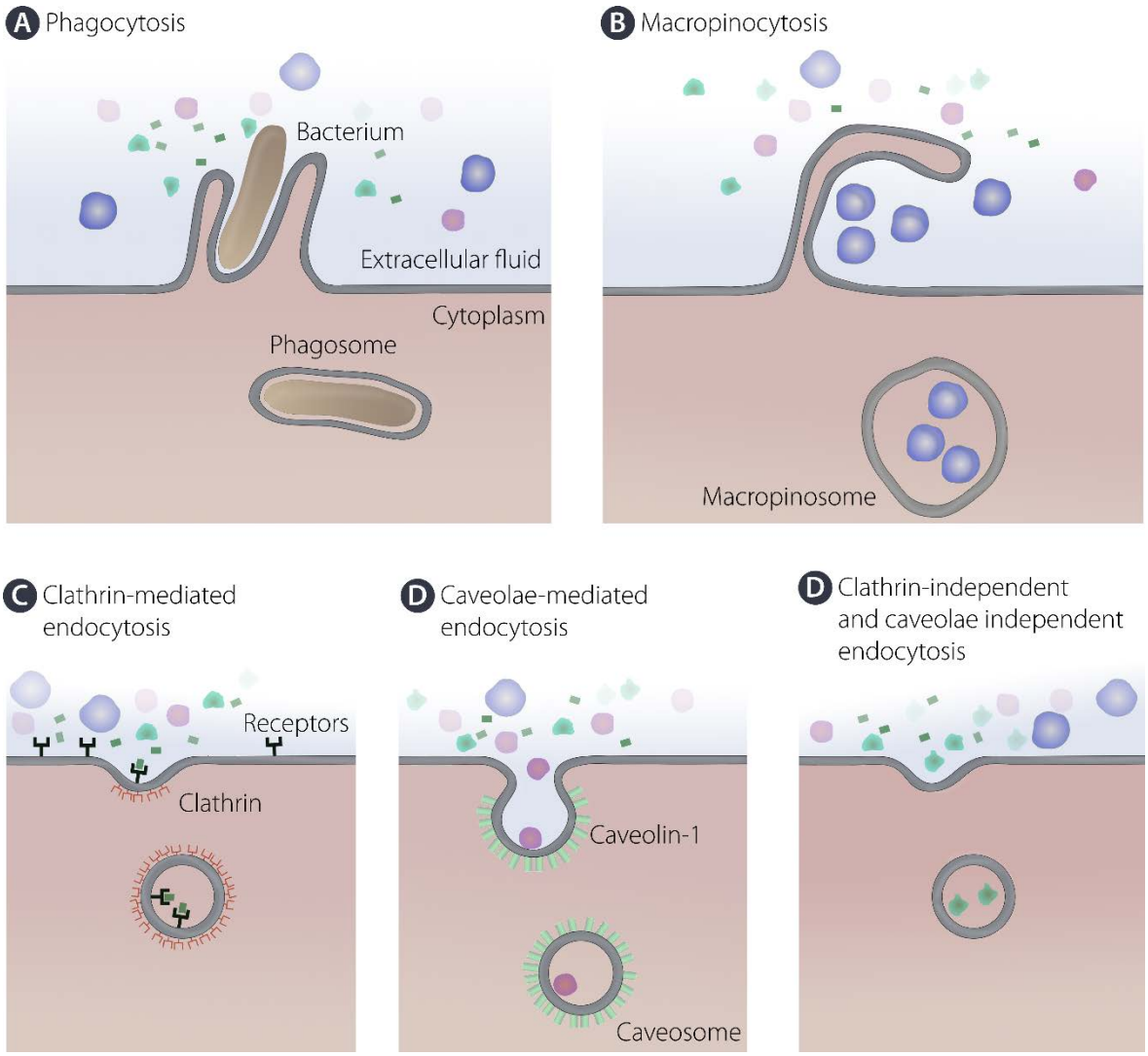

Figure 1.7 Uptake mechanisms of cells. Large particles such as bacteria are internalized by phagocytosis based on opsonization (**A**). Trafficking of particles can occur through nonspecific macropinocytosis (**B**). Multiple other uptake pathways are available. These include (**C**) clathrin-mediated endocytosis, (**D**) caveolae-mediated endocytosis, and (**E**) clathrin-independent and caveolae-independent endocytosis.

Considering intracellular drug delivery, it is worth stressing that the abovementioned mechanisms occur even without any specific targeting ligands on the nanobead's surface; they are based on the

innate functions of both professional and nonprofessional phagocytes and thus complicate drug delivery due to nonspecific targeting and rapid clearance. This can be avoided by both changing the NP surface energies and imposing immobilized steric barriers[57] and active targeting—modification of the NP surface with affinity ligands that are selective for certain receptors on the target cells. In the case of macrophage targeting, several approaches have been described. A typical example is mannose receptor-targeted delivery[65, 66].

1.4.2 Resident Phagocytes Migrate to the Infection Site

When an infection or inflammation occurs, professional phagocytes are attracted to the site by chemoattractants emitted by bacteria or other eukaryotic cells already present[67]. While this feature is one of the key players in both innate and adaptive immunity[68], it was found play an important role in the NP-treated infection scenario.

In vivo, it was described that NP-trafficking uninfected macrophages migrate to sites of infection, including the lungs in the case of TB (**Fig. 1.8**). Fenaroli and coworkers[69] observed that polymeric NPs injected into *Mycobacterium marinum*-infected zebrafish larvae were internalized into blood macrophages. Subsequently, these antitubercular NP-protected cells migrated to *M. marinum* granulomas. Similarly, in a rabbit model of TB, the dynamic influx of macrophages into granulomas was reported[70]. These reports support the concept that uninfected macrophages from distant sites may take up NPs and carry them to the infection site.

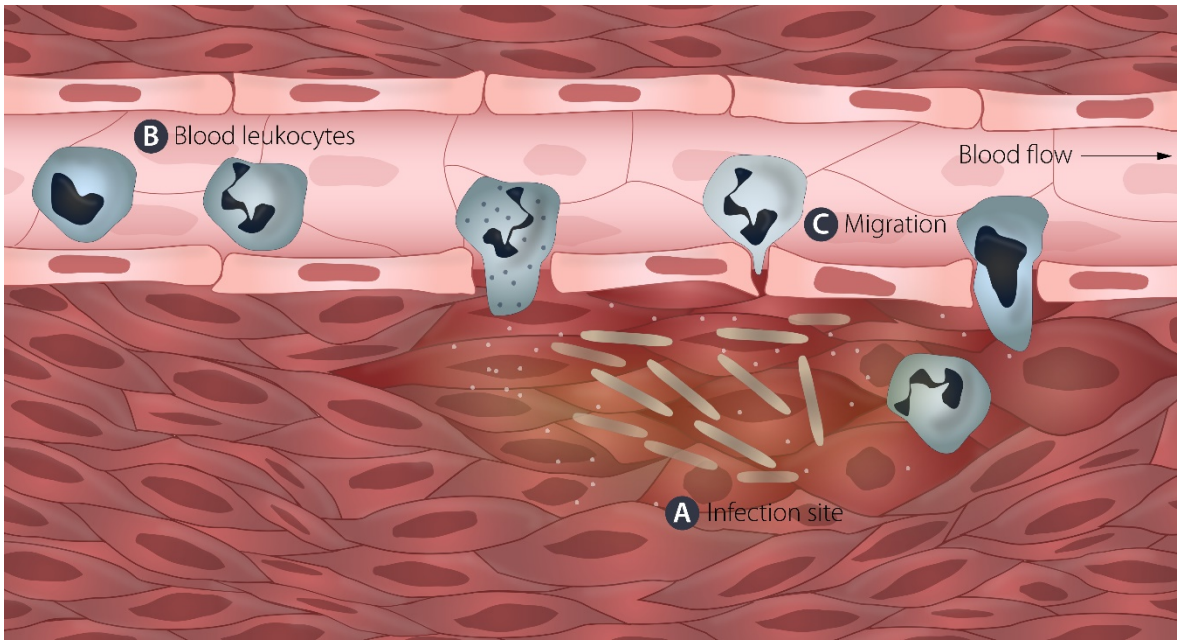

Figure 1.8 Cell migration to the infection site. In the case of an infection (**A**), leukocytes (including resident phagocytes) in the blood (**B**) respond to chemical attractants released by bacteria and chemical signals from injured cells (light dots). This results in leukocyte squeezing (**C**) between the blood vessel epithelial cells due to chemical signals (*i.e.*, positive chemotaxis).

1.4.3 Nanobeads Can Reach the Infection Site

In anticancer therapy, tumor-targeted drug delivery design is often based on an enhanced permeability and retention (EPR) effect. Due to the necessity for supplying oxygen and necessary nutrients to the tumor site, there is a need for rapid angiogenesis. Therefore, the neovasculature is usually leaky and abnormal in form and architecture—a feature allowing for the accumulation of macromolecules and nanobeads[71]. The upper size limit varies from below 100 nm to over 1 μm[72]. This phenomenon is not, however, exclusive to tumors but is also evident in infection[73, 74], where various factors (*e.g.*, bradykinin, nitric oxide, peroxynitrite, prostaglandins, *etc.*) mediate vascular permeability (**Fig. 1.9**) to facilitate the access of immune systems to the infected site. In the context of TB, the Griffiths group[75] described this phenomenon in a murine model of tuberculosis; fluorescently labeled liposomes extravasated from the vasculature after systemic administration and reached lung granulomas. Overall, the aspects emphasized formulate a logical strategy for anti-TB drug delivery and clearly justify the potential of nanobead-based interventions.

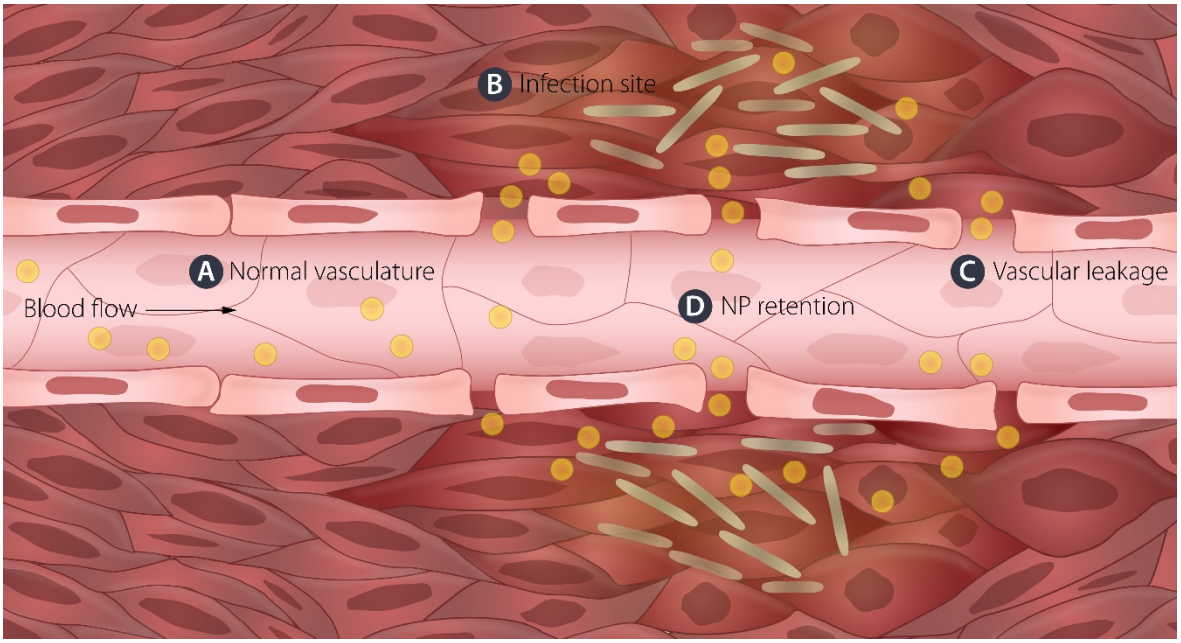

Figure 1.9 EPR effect in infection. Infection sites possess unique pathophysiological characteristics that are not observed in normal tissue (**A**). An infection (**B**) promotes a sustained biochemical cascade based on various biochemical factors. This mediates vascular permeability (**C**) and makes the vasculature leaky for macromolecules and NPs (yellow dots), allowing them for retention (**D**) within the infection site.

1.5 References

1. Thakur A., Mikkelsen H., Jungersen G. Intracellular Pathogens: Host Immunity and Microbial Persistence Strategies. *Journal of Immunology Research*. 2019, 2019, 1–24.
2. Macela A. *Infekční choroby a intracelulární parazitismus bakterií*. 1st ed. Prague: Grada, 2006. 216 p. ISBN 978-80-247-6338-5.
3. Kaufmann S.H.E. Intracellular pathogens: Living in an extreme environment. *Immunological Reviews*. 2011, 240 (1), 5–10.
4. Butts J.D. Intracellular Concentrations of Antibacterial Agents and Related Clinical Implications. *Clinical Pharmacokinetics*. 1994, 27 (1), 63–84.
5. Barry C.E., Mdluli K. Drug Sensitivity and Environmental Adaptation of Mycobacterial Cell Wall Components. *Trends in Microbiology*. 1996, 4 (7), 275–281.
6. Mihret A. The Role of Dendritic Cells in Mycobacterium Tuberculosis Infection. *Virulence*. 2012, 3 (7), 654–659.
7. Hunter R.L. Tuberculosis as a Three-Act Play: A New Paradigm for the Pathogenesis of Pulmonary Tuberculosis. *Tuberculosis (Edinburgh)*. 2016, 97, 8–17.
8. Amaral E.P., Lasunskaia E.B., D'Imperio-Lima M.R. Innate Immunity in Tuberculosis: How the Sensing of Mycobacteria and Tissue Damage Modulates Macrophage Death. *Microbes and Infection*. 2016, 18 (1), 11–20.
9. Nunes-Alves C., Booty M.G., Carpenter S.M., Jayaraman P., Rothchild A.C., Behar S.M. In Search of a New Paradigm for Protective Immunity to TB. *Nature Reviews Microbiology*. 2014, 12 (4), 289–299.
10. Gelperina S., Kisich K., Iseman M.D., Heifets L. The Potential Advantages of Nanoparticle Drug Delivery Systems in Chemotherapy of Tuberculosis. *American Journal of Respiratory and Critical Care Medicine*. 2005, 172 (12), 1487–1490.
11. Sosnik A., Carcaboso A.M., Glisoni R.J., Moretton M.A., Chiappetta D.A. New Old Challenges in Tuberculosis: Potentially Effective Nanotechnologies in Drug Delivery. *Advanced Drug Delivery Reviews*. 2010, 62 (4–5), 547-559.
12. Namukwaya E., Nakwagala F.N., Mulekya F., Mayanja-Kizza H., Mugerwa R. Predictors of Treatment Failure Among Pulmonary Tuberculosis Patients in Mulago Hospital, Uganda. *African Health Sciences*. 2011, 11 (1), S105–S111.
13. Panickar J.R., Hoskyns W. Treatment Failure in Tuberculosis. *European Respiratory Journal*. 2007, 29 (3), 561–564.
14. Trousil J., Ulmann V., Hruby M. Fluorescence & Bioluminescence in the Quest for Imaging, Probing & Analysis of Mycobacterial Infections. *Future Microbiology*. 2018, 13, 933–951.
15. Olaru I.D., von Groote-Bidlingmaier F., Heyckendorf J., Yew W.W., Lange C., Chang K.C. Novel Drugs Against Tuberculosis: A Clinician's Perspective. *European Respiratory Journal*. 2015, 45 (4), 1119.
16. Andersen P., Doherty T. The Success and Failure of BCG – Implications for a Novel TB Vaccine. *Nature Reviews Microbiology*. 2005, 3, 656–662.
17. Olusanya T.O.B., Haj Ahmad R.R., Ibegbu D.M., Smith J.R., Elkordy A.A. Liposomal Drug Delivery Systems and Anticancer Drugs. *Molecules (Basel, Switzerland)*. 2018, 23 (4), 907.
18. Paul W., Sharma C.P. Inorganic nanoparticles for targeted drug delivery. In: Sharma C.P., editor. *Biointegration of Medical Implant Materials*. 2nd ed. Sawston, Cambridge, UK: Woodhead Publishing, 2020. p. 333–373. ISBN 978-0-08-102680-9.
19. Naqvi S.T.R., Rasheed T., Hussain D., Najam ul Haq M., Majeed S., shafi S., et al. Modification Strategies for Improving the Solubility/Dispersion of Carbon Nanotubes. *Journal of Molecular Liquids*. 2020, 297, 111919.
20. Şen Karaman D., Kettiger H. Silica-Based Nanoparticles as Drug Delivery Systems: Chances and Challenges. In: Grumezescu A.M., editor. *Inorganic Frameworks as Smart Nanomedicines*. Norwich, New York: William Andrew Publishing, 2018. p. 1–40. ISBN 978-0-12-813661-4.
21. Bolhassani A., Javanzad S., Saleh T., Hashemi M., Aghasadeghi M.R., Sadat S.M. Polymeric Nanoparticles: Potent Vectors for Vaccine Delivery Targeting Cancer and Infectious Diseases. *Human vaccines & immunotherapeutics*. 2014, 10 (2), 321–332.
22. Adams M.L., Lavasanifar A., Kwon G.S. Amphiphilic Block Copolymers for Drug Delivery. *Journal of Pharmaceutical Sciences*. 2003, 92 (7), 1343–1355.
23. Martin C., Aibani N., Callan J.F., Callan B. Recent Advances in Amphiphilic Polymers for Simultaneous Delivery of Hydrophobic and Hydrophilic Drugs. *Therapeutic Delivery*. 2015, 7 (1), 15–31.

24. Xu Q., Li S., Yu C., Zhou Y. Self-assembly of Amphiphilic Alternating Copolymers. *Chemistry*. 2019, 25 (17), 4255–4264.
25. Singh A.N., Thakre R.D., More J.C., Sharma P.K., Agrawal Y.K. Block Copolymer Nanostructures and Their Applications: A Review. *Polymer-Plastics Technology and Engineering*. 2015, 54 (10), 1077–1095.
26. Li L., Raghupathi K., Song C., Prasad P., Thayumanavan S. Self-Assembly of Random Copolymers. *Chemical Communications*. 2014, 50 (88), 13417–13432.
27. Lele V.V., Kumari S., Niju H. Syntheses, Characterization and Applications of Graft Copolymers of Sago Starch – A Review. *Starch*. 2018, 70 (7–8), 1700133.
28. Deng Y., Zhang S., Lu G., Huang X. Constructing Well-Defined Star Graft Copolymers. *Polymer Chemistry*. 2013, 4 (5), 1289–1299.
29. Hong S.W., Gu W., Huh J., Sveinbjornsson B.R., Jeong G., Grubbs R.H., et al. On the Self-Assembly of Brush Block Copolymers in Thin Films. *ACS Nano*. 2013, 7 (11), 9684–9692.
30. Gopinath V., Saravanan S., Al-Maleki A.R., Ramesh M., Vadivelu J. A review of natural polysaccharides for drug delivery applications: Special focus on cellulose, starch and glycogen. *Biomedicine & Pharmacotherapy*. 2018, 107, 96–108.
31. Liu Y., Wang Z., Liu Y., Zhu G., Jacobson O., Fu X., et al. Suppressing Nanoparticle-Mononuclear Phagocyte System Interactions of Two-Dimensional Gold Nanorings for Improved Tumor Accumulation and Photothermal Ablation of Tumors. *ACS Nano*. 2017, 11 (10), 10539–10548.
32. Bettencourt A., Almeida A.J. Poly(methyl methacrylate) Particulate Carriers in Drug Delivery. *Journal of Microencapsulation*. 2012, 29 (4), 353–367.
33. Chan J.M., Valencia P.M., Zhang L., Langer R., Farokhzad O.C. Polymeric Nanoparticles for Drug Delivery. In: Grobmyer S.R., Moudgil B.M., editors. *Cancer Nanotechnology: Methods and Protocols*. Totowa, New Jersey: Humana Press, 2010. p. 163–175. ISBN 978-1-60761-609-2.
34. Haque S., Boyd B.J., McIntosh M.P., Pouton C.W., Kaminskas L.M., Whittaker M. Suggested Procedures for the Reproducible Synthesis of Poly(d,l-lactide-co-glycolide) Nanoparticles Using the Emulsification Solvent Diffusion Platform. *Current Nanoscience*. 2018, 14 (5), 448–453.
35. Schubert S., Delaney J., Schubert U. Nanoprecipitation and Nanoformulation of Polymers: From History to Powerful Possibilities beyond Poly(lactic acid). *Soft Matter*. 2011, 7, 1581–1588.
36. Amoabediny G., Haghiralsadat F., Naderinezhad S., Helder M.N., Akhoundi Kharanaghi E., Mohammadnejad Arough J., et al. Overview of Preparation Methods of Polymeric and Lipid-Based (Niosome, Solid Lipid, Liposome) Nanoparticles: A Comprehensive Review. *International Journal of Polymeric Materials and Polymeric Biomaterials*. 2018, 67 (6), 383–400.
37. Nasiruddin M., Neyaz M.K., Das S. Nanotechnology-Based Approach in Tuberculosis Treatment. *Tuberculosis Research and Treatment*. 2017, 2017, 4920209–4920209.
38. Kim C.K., Ghosh P., Pagliuca C., Zhu Z.-J., Menichetti S., Rotello V.M. Entrapment of Hydrophobic Drugs in Nanoparticle Monolayers with Efficient Release into Cancer Cells. *Journal of the American Chemical Society*. 2009, 131 (4), 1360–1361.
39. Kura A.U., Fakurazi S., Hussein M.Z., Arulselvan P. Nanotechnology in Drug Delivery: The Need for More Cell Culture Based Studies in Screening. *Chemistry Central journal*. 2014, 8, 46–46.
40. Mourdikoudis S., Pallares R.M., Thanh N.T.K. Characterization Techniques for Nanoparticles: Comparison and Complementarity Upon Studying Nanoparticle Properties. *Nanoscale*. 2018, 10 (27), 12871–12934.
41. Nobbmann U., Morfesis A. Light Scattering and Nanoparticles. *Materials Today*. 2009, 12 (5), 52–54.
42. Stetefeld J., McKenna S.A., Patel T.R. Dynamic Light Scattering: A Practical Guide and Applications in Biomedical Sciences. *Biophysical Reviews*. 2016, 8 (4), 409–427.
43. Wang L., Cheng H. Principles and Application of Laser Light Scattering (LLS) in Characterization of the Spatial Configuration of Microbial Products in Aqueous Solution. *Trends in Environmental Analytical Chemistry*. 2015, 8, 12–19.
44. Schärtl W. *Light Scattering from Polymer Solutions and Nanoparticle Dispersions*. 1st ed. Berlin: Springer Laboratory, 2007. 191 p. ISBN 978-3-540-71950-2.
45. Giddings J.C., Yang F.J., Myers M.N. Flow-Field-Flow Fractionation: A Versatile New Separation Method. *Science*. 1976, 193 (4259), 1244.
46. Pasti L., Dondi F., Contado C. Field-Flow Fractionation. In: Corradini D., editor. *Handbook of HPLC*. 2nd ed. Roca Raton, Florida: CRC Press, 2011. p. 329–358. ISBN 978-1-57444-554-1.
47. Zhang H., Lyden D. Asymmetric-Flow Field-Flow Fractionation Technology for Exomere and Small Extracellular Vesicle Separation and Characterization. *Nature Protocols*. 2019, 14 (4), 1027–1053.

48. Robin M.P., O'Reilly R.K. Strategies for Preparing Fluorescently Labelled Polymer Nanoparticles. *Polymer International*. 2015, 64 (2), 174–182.
49. Etrych T., Janoušková O., Chytil P. Fluorescence Imaging as a Tool in Preclinical Evaluation of Polymer-Based Nano-DDS Systems Intended for Cancer Treatment. *Pharmaceutics*. 2019, 11 (9), 471.
50. Garcia E., Shinde R., Martinez S., Kaushik A., Chand H.S., Nair M., et al. Cell-Line-Based Studies of Nanotechnology Drug-Delivery Systems: A Brief Review. In: Mohapatra S.S., Ranjan S., Dasgupta N., Mishra R.K., Thomas S., editors. *Nanocarriers for Drug Delivery*: Elsevier, 2019. p. 375–393. ISBN 978-0-12-814033-8.
51. Wang X., Xia Y., Liu L., Liu M., Gu N., Guang H., et al. Comparison of MTT Assay, Flow Cytometry, and RT-PCR in the Evaluation of Cytotoxicity of Five Prosthodontic Materials. *Journal of Biomedical Materials Research Part B*. 2010, 95 (2), 357–364.
52. ISO. *Biological evaluation of medical devices ISO 10993-5*. 3rd ed. Geneva: Internation Organization for Standardization, 2009. 34 p.
53. Adan A., Alizada G., Kiraz Y., Baran Y., Nalbant A. Flow Cytometry: Basic Principles and Applications. *Critical Reviews in Biotechnology*. 2017, 37 (2), 163–176.
54. Farmer J.R., DeLelys M. Flow Cytometry as a Diagnostic Tool in Primary and Secondary Immune Deficiencies. *Clinics in Laboratory Medicine*. 2019, 39 (4), 591–607.
55. Flores-Montero J., Kalina T., Corral-Mateos A., Sanoja-Flores L., Pérez-Andrés M., Martin-Ayuso M., et al. Fluorochrome Choices for Multi-Color Flow Cytometry. *Journal of Immunological Methods*. 2019, 475, 112618.
56. Imbuluzqueta E., Gamazo C., Ariza J., Blanco-Prieto M.J. Drug Delivery Systems for Potential Treatment of Intracellular Bacterial Infections. *Frontiers in Bioscience (Landmark Edition)*. 2010, 15, 397–417.
57. Gustafson H.H., Holt-Casper D., Grainger D.W., Ghandehari H. Nanoparticle Uptake: The Phagocyte Problem. *Nano Today*. 2015, 10 (4), 487–510.
58. Xiong L., Yamasaki S., Chen H., Shi L., Mo Z. Intracellular Growth and Morphological Characteristics of Legionella pneumophila during Invasion and Proliferation in Different Cells. *Biological and Pharmaceutical Bulletin*. 2017, 40 (7), 1035–1042.
59. Scordo J.M., Knoell D.L., Torrelles J.B. Alveolar Epithelial Cells in Mycobacterium tuberculosis Infection: Active Players or Innocent Bystanders? *Journal of Innate Immunity*. 2016, 8 (1), 3–14.
60. Foroozandeh P., Aziz A.A. Insight into Cellular Uptake and Intracellular Trafficking of Nanoparticles. *Nanoscale Research Letters*. 2018, 13 (1), 339-339.
61. Hirayama D., Iida T., Nakase H. The Phagocytic Function of Macrophage-Enforcing Innate Immunity and Tissue Homeostasis. *International Journal of Molecular Sciences*. 2017, 19 (1), 92.
62. Oh J.Y., Kim H.S., Palanikumar L., Go E.M., Jana B., Park S.A., et al. Cloaking Nanoparticles With Protein Corona Shield for Targeted Drug Delivery. *Nature Communications*. 2018, 9 (1), 4548.
63. Behzadi S., Serpooshan V., Tao W., Hamaly M.A., Alkawareek M.Y., Dreaden E.C., et al. Cellular Uptake of Nanoparticles: Journey Inside the Cell. *Chemical Society Reviews*. 2017, 46 (14), 4218–4244.
64. Kaksonen M., Roux A. Mechanisms of Clathrin-Mediated Endocytosis. *Nature Reviews Molecular Cell Biology*. 2018, 19 (5), 313–326.
65. Coya J.M., De Matteis L., Giraud-Gatineau A., Biton A., Serrano-Sevilla I., Danckaert A., et al. Tri-Mannose Grafting of Chitosan Nanocarriers Remodels the Macrophage Response to Bacterial Infection. *Journal of Nanobiotechnology*. 2019, 17 (1), 15–15.
66. Vieira A.C.C., Magalhães J., Rocha S., Cardoso M.S., Santos S.G., Borges M., et al. Targeted Macrophages Delivery of Rifampicin-Loaded Lipid Nanoparticles to Improve Tuberculosis Treatment. *Nanomedicine (London)*. 2017, 12 (24), 2721–2736.
67. Sokol C.L., Luster A.D. The Chemokine System in Innate Immunity. *Cold Spring Harbor Perspectives in Biology*. 2015, 7 (5), a016303.
68. Esche C., Stellato C., Beck L.A. Chemokines: Key Players in Innate and Adaptive Immunity. *Journal of Investigative Dermatology*. 2005, 125 (4), 615–628.
69. Fenaroli F., Westmoreland D., Benjaminsen J., Kolstad T., Skjeldal F.M., Meijer A.H., et al. Nanoparticles as Drug Delivery System against Tuberculosis in Zebrafish Embryos: Direct Visualization and Treatment. *ACS Nano*. 2014, 8 (7), 7014–7026.
70. Dannenberg A.M. Macrophage Turnover, Division and Activation Within Developing, Peak and "Healed" Tuberculous Lesions Produced in Rabbits by BCG. *Tuberculosis*. 2003, 83 (4), 251–260.
71. Kalyane D., Raval N., Maheshwari R., Tambe V., Kalia K., Tekade R.K. Employment of Enhanced Permeability and Retention Effect (EPR): Nanoparticle-Based Precision Tools for Targeting of Therapeutic and Diagnostic Agent in Cancer. *Materials Science and Engineering C*. 2019, 98, 1252–1276.

72. Bae Y.H., Park K. Targeted Drug Delivery to Tumors: Myths, Reality and Possibility. *Journal of Controlled Release*. 2011, 153 (3), 198–205.
73. Maeda H. Vascular Permeability in Cancer and Infection as Related to Macromolecular Drug Delivery, With Emphasis on the EPR Effect for Tumor-Selective Drug Targeting. *Proceedings of the Japan Academy: Series B*. 2012, 88 (3), 53–71.
74. Azzopardi E.A., Ferguson E.L., Thomas D.W. The Enhanced Permeability Retention Effect: A New Paradigm for Drug Targeting in Infection. *Journal of Antimicrobial Chemotherapy*. 2012, 68 (2), 257–274.
75. Fenaroli F., Repnik U., Xu Y., Johann K., Van Herck S., Dey P., et al. Enhanced Permeability and Retention-Like Extravasation of Nanoparticles From the Vasculature Into Tuberculosis Granulomas in Zebrafish and Mouse Models. *ACS Nano*. 2018, 12 (8), 8646–8661.

CHAPTER 2: BLOCK COPOLYMER INVESTIGATION

Amphiphilic nanobead-based polymeric systems can be based on both block and graft copolymers, comprising hydrophilic and hydrophobic character that leads to favorable self-association properties. Block and graft copolymers represent systems that are highly tunable and often synthesized to be stimulus-responsive[1-3]. While the assembly of graft copolymers and their prediction are, as opposed to linear block copolymers, more complex, block copolymers represent a relatively simple approach; their self-assembly behavior can be controlled by the weight ratio of the hydrophilic and hydrophobic components.

In the context of TB treatment, we designed lipase-degradable and biocompatible nanoparticles based on the well-established methoxy poly(ethylene oxide)-*block*-poly(ε-caprolactone) (MPEO-*b*-PCL) copolymer capable of self-association into NPs carrying rifampicin (RIF), a first-line antitubercular agent.

The objective was to study the physicochemical and biorelevant properties (*i.e.*, cytotoxicity, biodegradability, anti-TB activity, pharmacokinetics, *etc.*) of such NPs and to critically cross-correlate physico-chemical and biological properties of such nanoparticles. Below, a commented summary that references publications [**P1**–**P3**] is shown.

2.1 Block Copolymer NPs for TB Treatment

2.1.1 Copolymer Synthesis and Characterization

For the purposes of this thesis, five different MPEO-*b*-PCL copolymers were prepared by a metal-free ring-opening polymerization of ε-caprolactone (CL) initiated by MPEO, where HCl was used as the catalyst (**Fig. 2.1A**).

All the MPEO-*b*-PCL copolymers were characterized by ^{1}H NMR spectroscopy and GPC. Both the ^{1}H NMR spectrum and normalized GPC curves are depicted in **Fig. 2.1**; the macromolecular characteristics of the copolymers are shown in **Table 2.1**.

Table 2.1 Chemical and molecular weight characterization of fabricated MPEO-*b*-PCL copolymers.

Copolymer[a]	M_n[b]	M_w[c]	M_n[c]	$Đ$[d]
$MPEO_{44}$-*b*-PCL_{18}	4 000	6 400	5 500	1.17
$MPEO_{44}$-*b*-PCL_{27}	5 000	6 700	5 400	1.23
$MPEO_{44}$-*b*-PCL_{81}	11 200	18 300	15 200	1.21
$MPEO_{113}$-*b*-PCL_{33}	8 800	8 300	7 200	1.16
$MPEO_{113}$-*b*-PCL_{113}	17 900	19 200	16 000	1.19

[a] Subscript indicates the calculated number of repeating units of the block polymer.
[b] Molecular weight values (Da) were determined using ^{1}H NMR.
[c] Molecular weight values (Da) were determined by GPC calibrated with polystyrene standards.
[d] Dispersity, M_w/M_n
Taken from [**P1**].

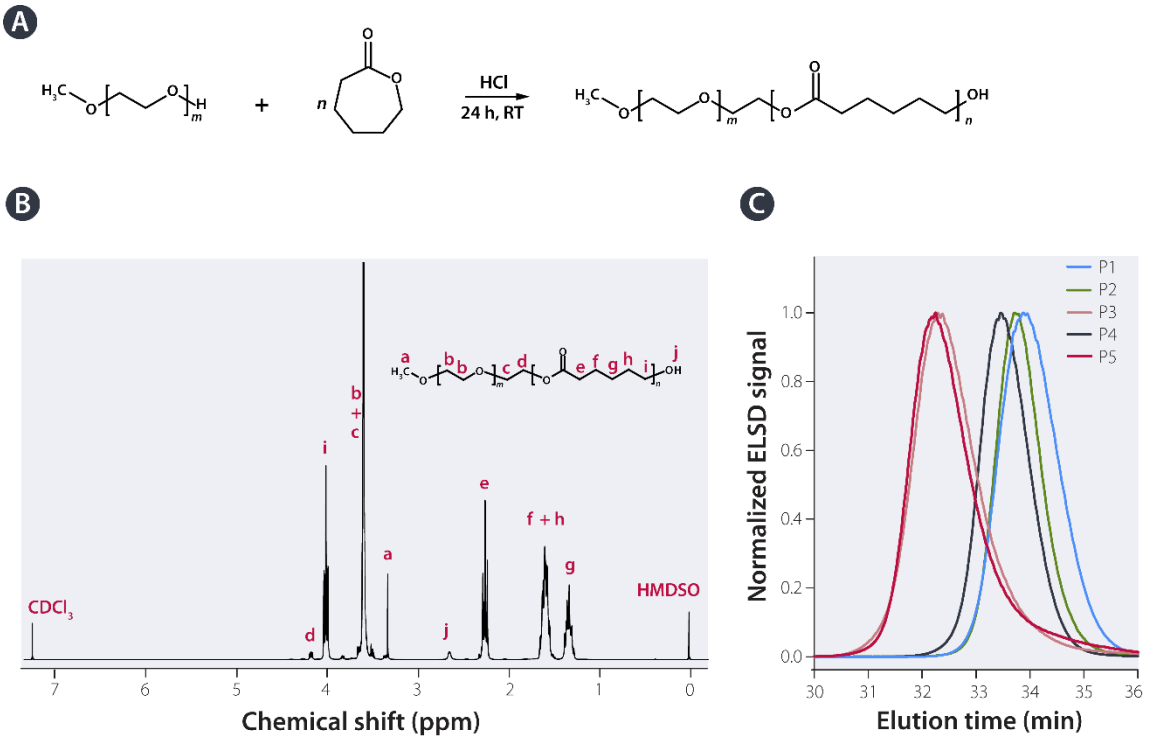

Figure 2.1 Block copolymer synthesis and characterization. (**A**) The copolymers were prepared by ring-opening copolymerization at room temperature (RT). (**B**) Typical ^{1}H NMR spectrum. Sample $MPEO_{44}$-*b*-PCL_{18} is shown. (**C**) GPC curves of prepared copolymers. Polymer P1, $MPEO_{44}$-*b*-PCL_{18}; P2, $MPEO_{44}$-*b*-PCL_{27}; P3, $MPEO_{44}$-*b*-PCL_{81}; P4, $MPEO_{113}$-*b*-PCL_{33}; P5, $MPEO_{113}$-*b*-PCL_{113}. Taken from [**P1**].

2.1.2 Self-assembly and NP characterization

As evident in publication [**P1**], all the copolymers prepared were subjected to self-assembly and NP characterization. The results below are, however, based on one representative, namely, the most promising nanoformulation based on $MPEO_{113}$-*b*-PCL_{33}. As was done with all the copolymers fabricated, the copolymer $MPEO_{113}$-*b*-PCL_{33} was subjected to nanoprecipitation from an acetone solution to prepare both the RIF-loaded and RIF-free samples (herein referred to as **NPs-RIF** and **NPs**). The loading efficacy was assessed *via* both drug loading (DL, %) and entrapment efficacy (EE, %) as described in detail [**P1**]. By way of UV/VIS spectrometry at 477 nm, using the following equations, DL and EE were found to be approximately 11 and approximately 15%, respectively.

$$\mathrm{DL} = \frac{\text{mass of the drug contained in nanoparticles}}{\text{mass of the nanoparticles containing drug}} \times 100 \tag{7}$$

$$\mathrm{EE} = \frac{\text{mass of the drug in nanoparticles}}{\text{mass of the drug used for the formulation}} \times 100 \tag{8}$$

Both the **NPs** and **NPs-RIF** formulations were comprehensively characterized by several methods in terms of size, size distribution, and morphology. As is evident from **Fig. 2.2A**, the dynamic light scattering (DLS) distribution functions are portrayed as one distribution mode with hydrodynamic diameter (D_h, nm) values of 75 nm and 85 nm for **NPs** and **NPs-RIF**, respectively. In contrast, small-angle neutron scattering (SANS) investigations revealed a slightly different average diameter for these two formulations: 54 nm for the **NPs** and 48 nm for the **NPs-RIF** samples.

This difference probably makes sense, as DLS also effectively measures the non-free water in proximity to the particle surface. Note that asymmetric flow field flow fractionation (AFFFF) results [**P1**] are in

line with those obtained from SANS; **NPs** and **NPs-RIF** formulations revealed diameters of gyration (D_g, nm) of 51 and 53 nm, supporting the fact that DLS can overestimate the actual size distributions of nanoparticles[4, 5]. In addition, the SANS results show a complete overlap at high q, suggesting that the internal NP structure does not change after RIF loading. Additionally, there was no difference in the SANS data obtained at 25 °C and 37 °C, demonstrating that the nanoformulations prepared are of very good temperature stability.

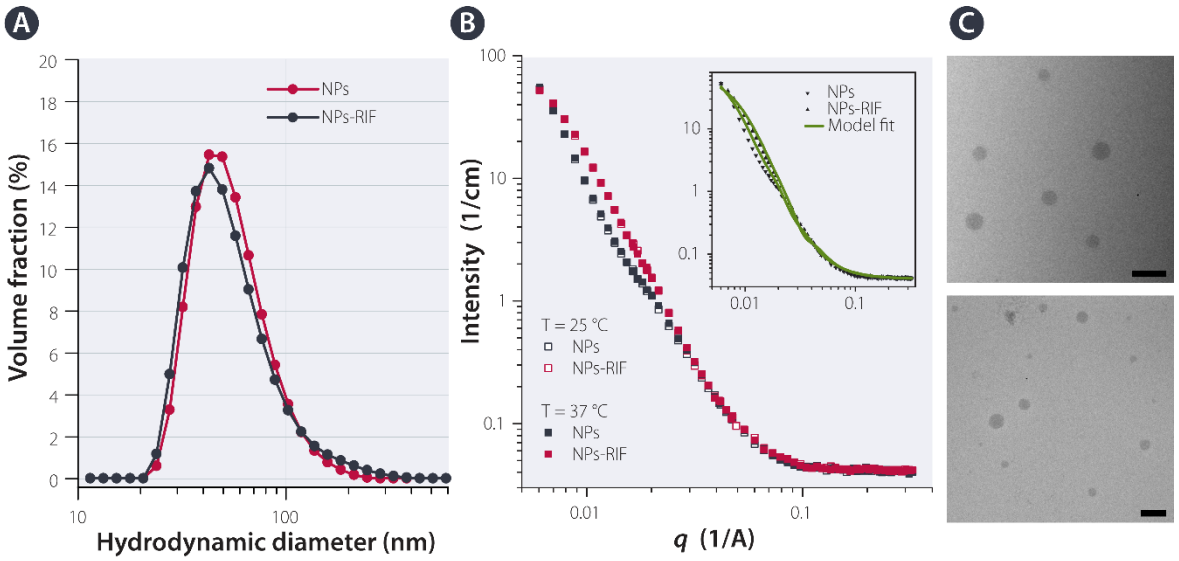

Figure 2.2 NP characterization. (**A**) Volume-weighted size distribution functions. (**B**) Small-angle neutron scattering (SANS) patterns. (**C**) Cryo-TEM images of blank (top) and RIF-loaded NPs (bottom). Scale bars: 100 nm. Taken from [**P2**].

2.2 Testing on a Cellular Level

2.2.1 Cytotoxicity and Cellular Internalization

Regarding biological activity, we studied the main aspects related to the interaction of our nanocarrier with the biological environment. First, the use of NP interventions bears the risk of side effects. Within the biorelevant analysis, cytotoxicity and compatibility were evaluated using the MTT assay. This assay is based on the cleavage of the yellow tetrazolium salt MTT to blue formazan crystals by metabolically active cells. **Fig. 2.3** depicts the results from testing with the mouse ascites-based macrophage J774A.1 and Raw 264.7 cell lines, the mouse peritoneal macrophage IC-21 cell line, the mouse alveolar macrophage MH-S cell line, and the human lung epithelium BEAS-2B cell line. In accordance with the fact that MPEO-*b*-PCL is an FDA-approved copolymer, blank $MPEO_{113}$-*b*-PCL_{33} showed no significant cytotoxicity for all the cell lines used. In contrast, for all the cell lines used, the **NPs-RIF** formulation led to increased cytotoxicity compared to free **RIF**. Note that this finding is, in terms of drug delivery, somewhat unusual, as nanomedicines are known to decrease the toxicity of drugs. It can be hypothesized, however, that this phenomenon is caused by a more efficacious RIF delivery to macrophages. The half maximal inhibitory concentration (IC_{50}, µg/mL) values for the **NPs-RIF** were found to be 238 ± 27, 134 ± 5, 94 ± 7, 157 ± 6 and 273 ± 20 for the IC-21, J774A.1, Raw 264.7, MH-S and BEAS-2B cell lines, respectively. It can thus be suggested that our nanoformulation should not lead to significant toxic effects *in vivo*, as the estimated IC50 values are significantly higher than the clinical concentrations of RIF.

Considering the NP size estimated (see above), the NPs obtained should be suitable for internalization into macrophages. This was proven by confocal laser scanning microscopy investigation with IC-21 peritoneal macrophages. **Fig. 2.4** depicts the trafficking of MPEO-*b*-PCL nanoparticles covalently labeled with 7-(diethyl amino)coumarin-3-carbonyl azide (DACCA). It is evident that internalization is a fast process; the cell fluorescence plateau was reached within several minutes. Note that this is in line with flow cytometry investigations that are discussed in publications [**P1**, **P3**].

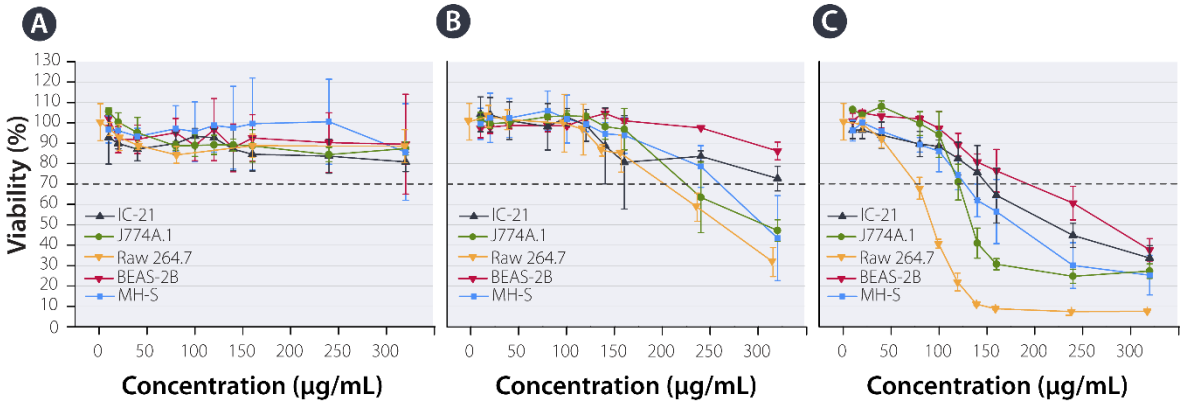

Figure 2.3 Results of cytotoxicity testing. IC-21 (murine peritoneal macrophages), J774A.1 and Raw 264.7 (murine ascites-based macrophages), BEAS-2B (human lung epithelial cells), and MH-S (murine alveolar macrophages) cells were incubated with different concentrations of the studied formulations for 24 h, and their viability was assessed using the MTT assay. Effect of RIF-free MPEO-*b*-PCL nanoparticles (**A**, **NPs**), free RIF (**B**), and RIF-loaded formulation (**C**, **NPs-RIF**). The horizontal lines in the panels indicate a cell viability level where the data above are considered noncytotoxic and below cytotoxic. Taken from [**P1**, **P2**].

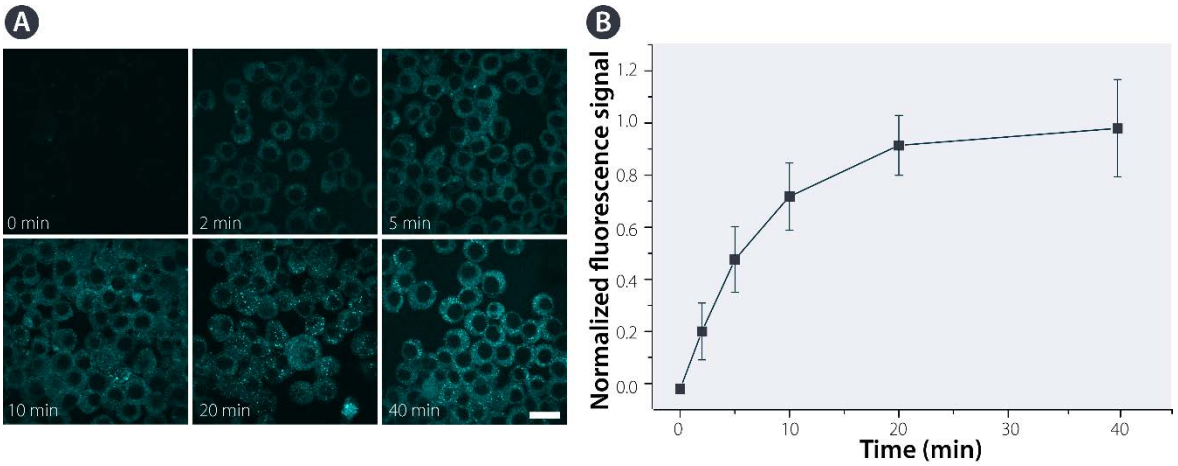

Figure 2.4. The incubation time-dependent internalization of DACCA-labeled MPEO-*b*-PCL **NPs** by IC-21 macrophages. (**A**) Confocal laser scanning microscopy images of peritoneal macrophages after the addition of the MPEO-*b*-PCL nanoformulation (40 µg/mL). Scale bar: 20 µm. (**B**) The corresponding signal quantification. Taken from [**P2**].

2.2.2 Macrophage Infection and Treatment

To assess the antitubercular efficacy in mycobacteria-infected macrophages, we infected Raw 264.7 cells with the virulent *M. tuberculosis* H37Rv strain and treated them with the **NPs-RIF** formulation. Subsequently, the cells were lysed, and the cell lysates were seeded on cultivation plates. The efficacy was analyzed by way of numbering colony forming units (CFUs). **Fig. 2.5A** depicts an experiment in which the Raw 264.7 cells were treated at a concentration of 20 µg/mL (corresponding to free RIF equivalents) for 5 days. It was found that the nanobead-based intervention carrying RIF is significantly more efficacious than free RIF. In other words, no H37Rv colonies grew on the Löwenstein–Jensen

plates after nondiluted cell lysate was seeded. In the case of free **RIF** treatment, the infection still persisted after 5 days of monotherapy.

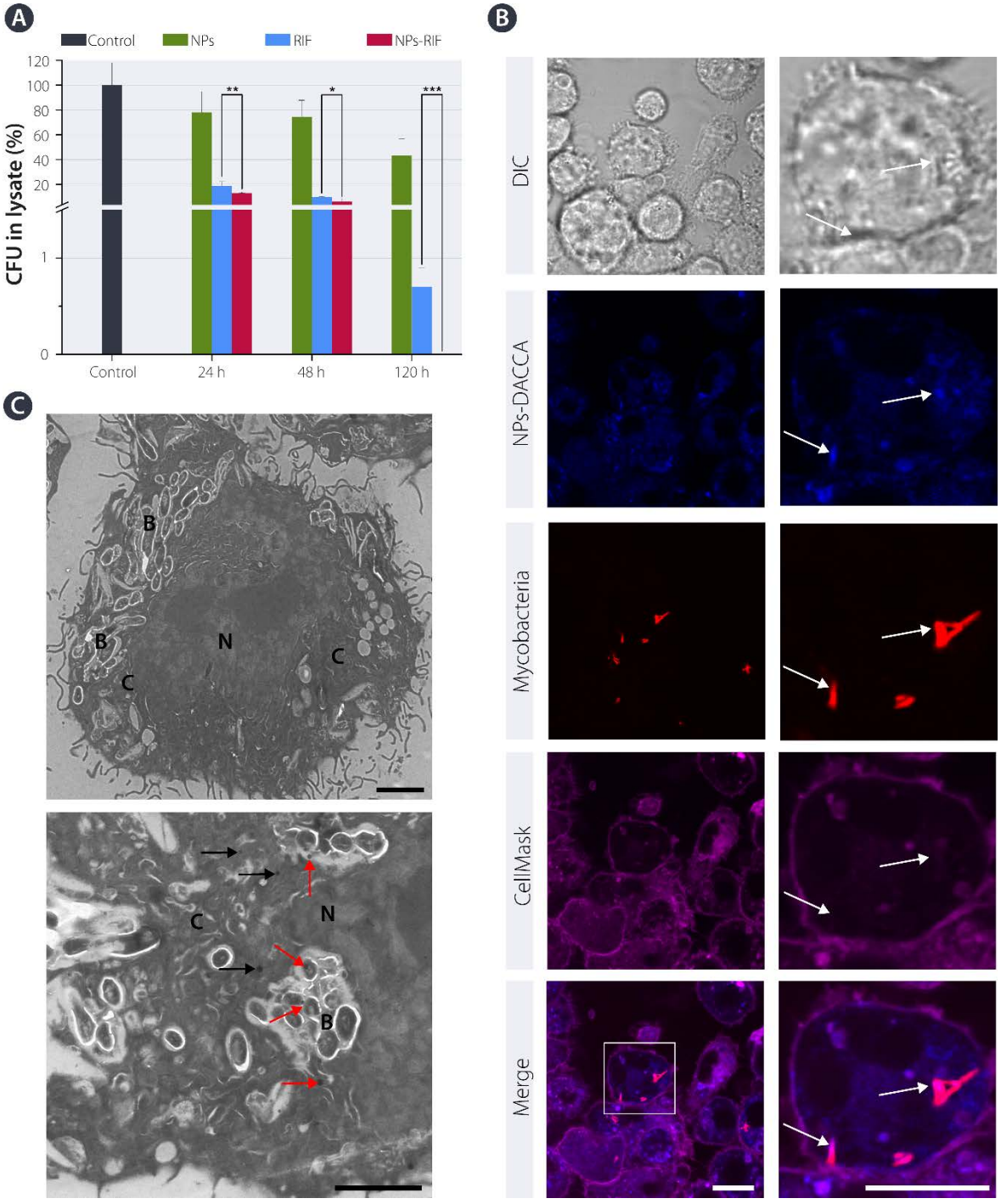

Figure 2.5 Infection and treatment of Raw 264.7 macrophages. (**A**) Killing effects of **NPs-RIF** during a five-day treatment procedure. Note the higher efficiency of RIF-loaded nanoparticles. (**B**) Corresponding images from confocal laser scanning microscopy of Raw 264.7 cells after infection by DsRed-expressing *M. bovis* BCG and one day of treatment with DACCA-labeled NPs. Note the increased NP-related signal within the location of mycobacteria persistence (white arrows). Scale bars: 10 µm. DIC – differential interference contrast. (**C**) Corresponding micrographs from TEM ultrastructural analysis. Examples are from a mycobacteria-infected cell that was treated with NPs overnight. Conventional TEM demonstrated the occurrence of bacteria in the cytoplasm, as well as their frequent association with NPs (red arrows). NPs distributed freely in the cytoplasm are marked with black arrows. B – bacteria, C – cytoplasm, N – nucleus. Scale bars: 2 µm. Taken from [**P1**].

As emphasized in [**P7**], fluorescent protein-expressing mycobacteria represent an elegant tool for probing and analyzing mycobacterial infections and antitubercular drug delivery systems. Infection experiments with red fluorescent protein-expressing *M. bovis* Calmette–Guérin (BCG) allowed us to elucidate the treatment procedure. For this purpose, DACCA-labeled NPs were incubated with fluorescent *M. bovis* BCG-infected Raw 264.7 cells overnight. The results from this *in vitro* experiment proved that our nanobead-based intervention is taken up by both healthy and infected cells, suggesting that this MPEO-*b*-PCL-based drug delivery system can be adapted into a platform for delivering antituberculotics into infected macrophages (**Fig. 2.5B**). Note that the presence of the MPEO-*b*-PCL assemblies was also confirmed by ultrastructural analysis using TEM investigation (**Fig. 2.5C**).

2.3 Testing in Animal Models

2.3.1 Testing in Zebrafish: Imaging and Infection

To assess the *in vivo* efficacy of our system, we started with zebrafish (*Danio rerio*), which is an attractive vertebrate model organism for studying TB, as it is sensitive to *M. marinum*[6], the causative agent of tuberculosis in ectotherms, including fish. We used this model for the noninvasive study of fate *in vivo* and simultaneous testing of the antitubercular properties of **NPs-RIF**. For the *in vivo* imaging, we injected Tg(*fli1*a:EGFP) zebrafish larvae possessing vasculature visible by way of green fluorescence with tetramethylrhodamine-5-carbonyl azide (TMR)-labeled $MPEO_{113}$-*b*-PCL_{33} NPs into the caudal vein. As depicted in **Fig. 2.6**, the majority of the TMR-labeled NPs colocalized with endothelial cells within 2 h of the injection.

Subsequently, we infected zebrafish embryos with *M. marinum*. It is known that such an infection results, similar to human tuberculosis, in uptake by macrophages that aggregate over time to form granulomas[7, 8]. Thus, we injected approximately 160 CFU of *M. marinum*; one day post infection, the larvae received an injection containing 10 ng of RIF in either free form or encapsulated in NPs, and cumulative mortality was estimated.

Despite the fact that the majority of the NPs were found in the endothelial cells, which are not the primary sites of mycobacterial persistence, treatment by NPs-RIF led to significant improvement of the treatment compared to free RIF (**Fig. 2.6C**), suggesting that there could be similar potential in terms of testing with a mammalian infection model (*e.g.*, mice).

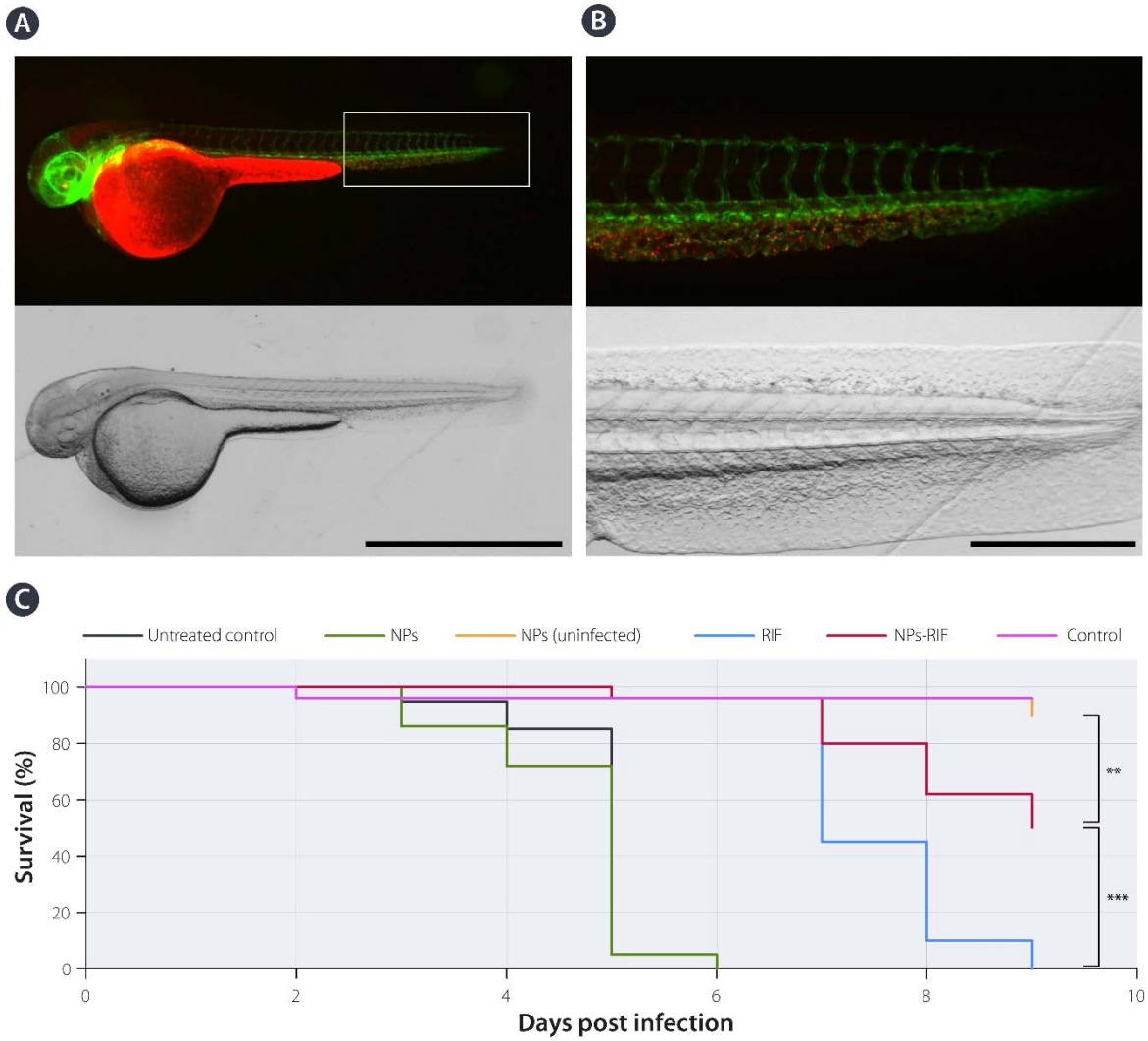

Figure 2.6 Zebrafish model of tuberculosis. (**A**) Micrographs of Tg(*fli1*a:EGFP) zebrafish embryos injected with red fluorescent NPs. Green channel: blood vessels; red channel: TMR-labeled NPs, in addition to autofluorescence from the yolk sack. Scale bar: 1 mm. (**B**) Enlargement of the area demarcated by the white rectangle, showing the fluorescent image of the tail area. The NPs, in red, clearly colocalize with endothelial cells, causing the majority to no longer circulate in the bloodstream. Scale bar: 300 µm. (**C**) Cumulative mortality of infected zebrafish larvae treated with 10 mg/kg free **RIF**, **NPs-RIF** and blank nanoparticles (**NPs**). Taken from [**P1**].

2.3.2 Testing in Mice: Bioimaging and Pharmacokinetics Study

To obtain a more detailed picture of this system, we evaluated the biodistribution and pharmacokinetics of the $MPEO_{113}$-*b*-PCL_{33} NPs in mice.

First, *in vivo* and *ex vivo* imaging of near-infrared (NIR) fluorescent dye Dyomics 700-labeled NPs (referred to as **NPs-Dy**) was carried out after a single intraperitoneal (i.p.) injection into mycobacteria-free BALB/c mice at a dose of 10 mg/kg, an amount corresponding to the dose used for all the mouse

experiments described below. **Fig. 2.7A** shows the NIR signal of **NPs-Dy** and free **Dy** (administered at a corresponding concentration). After the maximum whole-body NIR signal was reached within 1–2 h after the administration of both **NPs-Dy** and **Dy**, the free dye revealed faster clearance. The decay of the **NPs-Dy** signal was slower, as evident from the NIR data quantification (**Fig. 2.7B**). Regarding the fate of the NPs, the bioimaging experiment revealed that the NPs were found mainly in the liver and intestinal tissue, *i.e.*, organs of the mononuclear phagocyte system (MPS). This is in line with additional *ex vivo* imaging 6 h after administration (**Fig. 2.7C**), suggesting that both liver and intestinal tissue are involved in NP elimination and that the polymer is cleared via both the MPS and the hepatobiliary system.

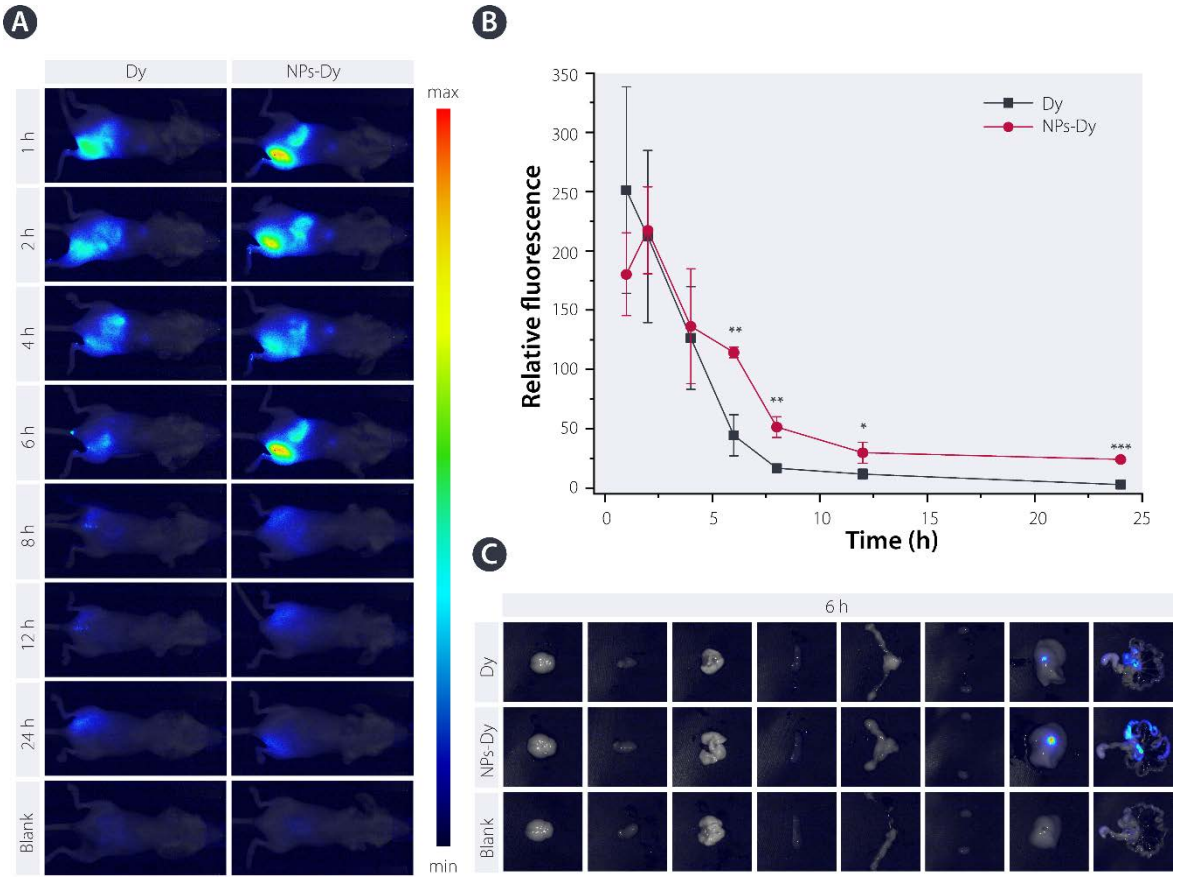

Figure 2.7 Bioimaging of the NP intervention in BALB/c mice after intraperitoneal administration. (**A**) Real-time imaging within 24 h after administration. (**B**) Whole body NIR fluorescence data quantification ($n = 3$). Note the prolonged elimination of the NP-based intervention (**NPs-Dy**) compared to the free Dyomics 700 (**Dy**). (**C**) *Ex vivo* imaging of brain, heart, lung, spleen, bladder/ovary, kidney, liver, and stomach/intestine (from left to right) at 6 h after administration. Liver-related fluorescence intensities were 1.7 ± 1.5 and 12.9 ± 5.6 for **Dy** and **NPs-Dy**, respectively, whereas intestinal tissue revealed fluorescence intensities of 8.8 ± 0.3 and 40.8 ± 15.0 for **Dy** and **NPs-Dy**, respectively. The results are expressed as the mean ± SD and were analyzed by ANOVA; for bioimaging, three mice were used for each time point. Taken from [**P2**].

To assess the pharmacokinetics, RIF levels in both serum and lung tissue were studied by HPLC coupled with mass spectrometry. For this, a single dose of RIF in either free form or encapsulated in NPs was administered (10 mg/kg, i.p.). At various time points (2, 4, 6, 8, 12, 24, 48, and 72 h), blood and lungs were collected and analyzed.

It is evident that both serum and lung homogenate analysis revealed that **NPs-RIF** showed a sustained release compared to free RIF (**Fig. 2.8A** and **2.8B**); this appears to be in accordance with

the prolonged retention proven by the bioimaging (see above). Consistently, RIF released from the NPs-RIF had significantly higher AUCs for both serum and lung tissue than free RIF (**Table 2.2**). This suggests that the bioavailability was increased in the case of the nanoformulation.

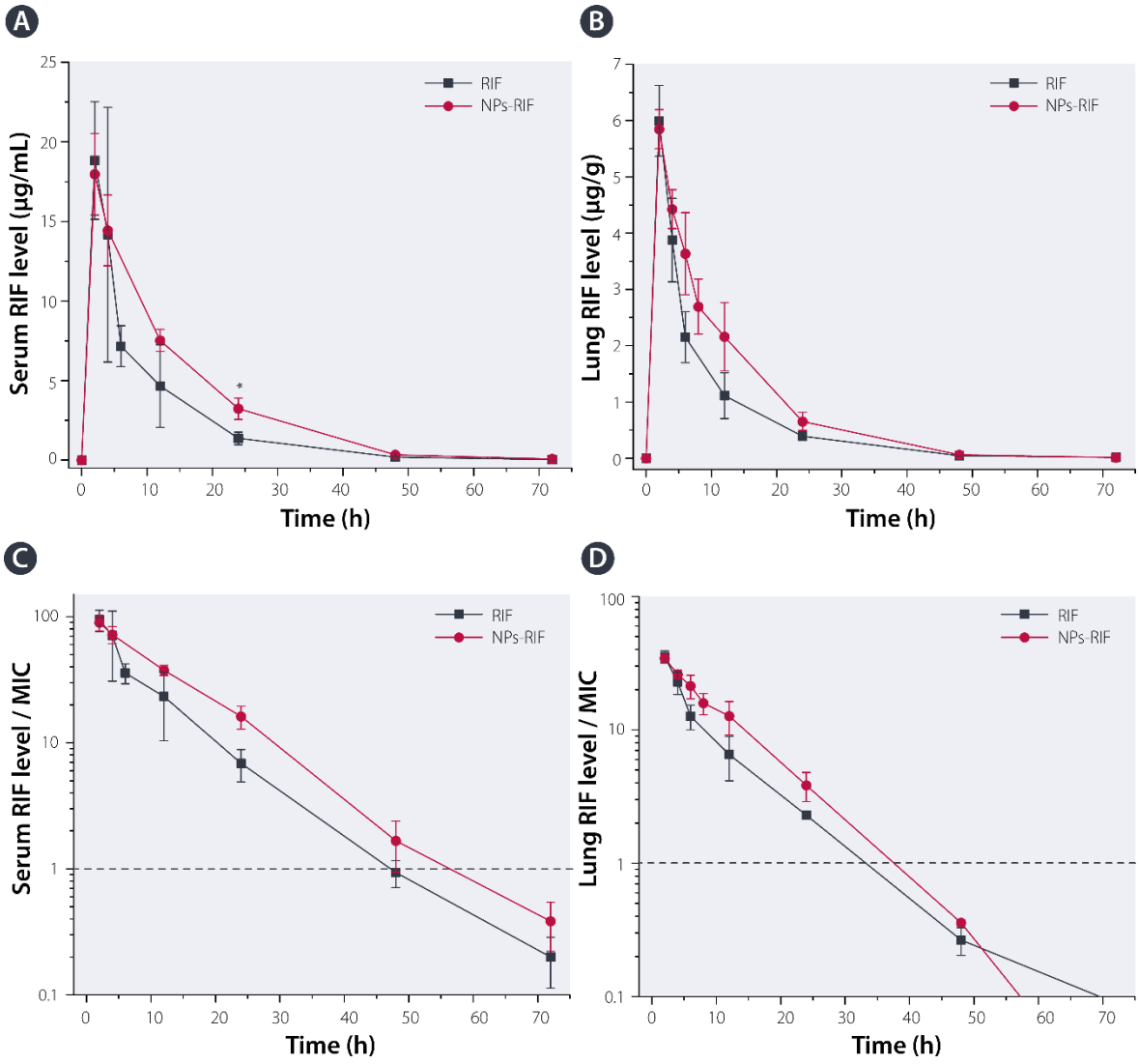

Figure 2.8 Pharmacokinetics and pharmacodynamics. **NPs-RIF** and free **RIF** were administered intraperitoneally to mice at a dose of 10 mg/kg rifampicin. The animals were euthanized at various time points to determine the rifampicin pharmacokinetics in the serum (**A**) and lungs (**B**). The pharmacodynamics of **NPs-RIF** and free **RIF** as expressed by the ratio of the RIF level in serum (**C**) and lungs (**D**) and the minimum inhibitory concentration (MIC) of 0.2 µg/mL. The volume distribution of rifampicin (0.85 L/kg) was used to convert MIC to a more tissue-relatable value (0.17 µg/g). The horizontal lines represent a ratio of 1.

In microbiology, the lowest concentration of an antimicrobial agent that inhibits the visible growth of a microorganism (minimum inhibitory concentration, MIC) is an important parameter. Thus, for the pharmacodynamics discussion, AUC_{0-24h}/MIC and C_{max}/MIC ratios were calculated. The C_{max}/MIC ratios were found to be almost the same for both **NPs-RIF** and free **RIF** (**Table 2.2**). However, the level of RIF released from the nanobead-based intervention in both serum and lungs was greater than that of free RIF, and hence, the nanobead-based intervention-related T > MIC (*i.e.*, the time during which the drug level is above the MIC) was greater in both serum and lungs (**Fig. 2.8B** and **2.8C**). This suggests that the pharmacodynamics (as expressed by the ratio of the RIF concentration to the MIC) of RIF were

improved when RIF was carried by NPs. Similarly, the **NPs-RIF**-related $AUC_{0-24\ h}$/MIC ratios were greater than those found for free RIF (**Table 2.2**) in both serum and lungs. Altogether, these results suggested a successful treatment outcome *in vivo*.

Table 2.2 Summary of critical pharmacokinetic and pharmacodynamic values for **RIF** and **NPs-RIF**

Organ	System	$AUC_{0-24\ h}$	AUC_{total}	C_{max}	T_{max} (h)	$T_{1/2}$ (h)	C_{max}/MIC	$AUC_{0-24\ h}$/MIC (h)
Serum	RIF	144.8	163.5	18.8	2	3.8	94	724
	NPs-RIF	202.7	250.5	18.0	2	8.3	90	1 013.5
Lung	RIF	40.7	46.6	6.0	2	3.2	35.2	239.4
	NPs-RIF	57.1	66.6	5.8	2	6.4	34.1	335.9

Definition of abbreviations: $AUC_{0-24\ h}$, area under the concentration–time curve from 0 to 24 h after dose, units are µg·h/mL or µg·h/g for serum or lung tissue, respectively; AUC_{total}, area under the concentration–time curve from 0 to 72 h after administration; C_{max}, maximum concentration in serum or lung tissue (µg/mL or µg/g, respectively); T_{max}, time to maximum concentration; $T_{1/2}$, elimination half-life; MIC, minimal inhibitory concentration. The results obtained are based on sampling at 2, 4, 6, 8, 12, 24, 48, and 72 h after a single intraperitoneal dose (10 mg/kg). Taken from [**P2**].

2.3.3 Testing in Mice: Infection and Treatment

Because of the promising results from the *in vitro* and *in vivo* investigations, we focused on the antitubercular efficiency of our system in a mouse model of pulmonary tuberculosis. An intranasal infection with virulent *M. tuberculosis* H37Rv was carried out using BALB/c mice; the animals received 250–900 viable tubercle bacilli, resulting in well-defined lung granulomas (**Fig. 2.9**) over the ensuing four weeks.

Four weeks post infection, the animals were treated with blank NPs, free RIF, and NPs-RIF via the i.p. route (10 mg/kg), 5 days per week. Note that the dose used represents an amount that has been equated to be a clinically tolerated dose for RIF in humans. As depicted in **Fig. 2.9**, the tubercle burden in mice treated with **NPs-RIF**, compared to untreated mice, was significantly reduced in the lungs after both 4 and 8 weeks. Moreover, the reductions in CFU in lung tissue achieved by the **NPs-RIF** intervention were significantly greater than that achieved by an equivalent dose of free **RIF**. Note that treatment with blank NPs did not reveal any notable effect on infection reduction.

The results were also confirmed by histopathological examinations (**Fig. 2.10**); after 12 weeks post infection, both the untreated animals and the blank **NPs**-treated mice developed chronic inflammation with nodular granulomatous reaction with numerous acid-fast bacilli (*i.e.*, mycobacteria) and collagen deposition. In contrast, both **NPs-RIF**- and **RIF**-treated mice presented lungs with a reduced number of granulomas and decreased collagen deposition. These findings suggest the suppression of nodular chronic inflammation.

Note that histopathological examinations of liver, kidney, and brain dissected from the blank **NPs**-treated animals revealed no morphological differences from the untreated healthy mice.

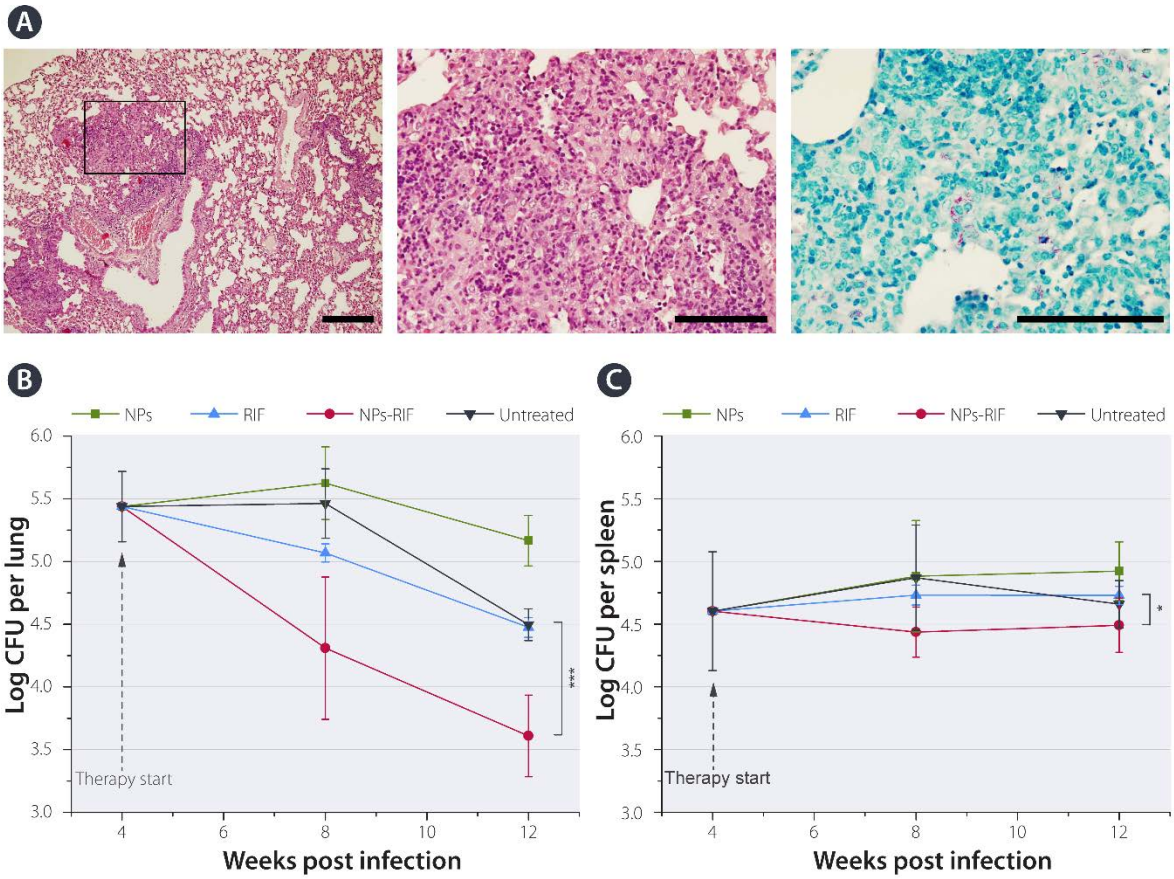

Figure 2.9 *In vivo* testing of the MPEO-*b*-PCL NPs. BALB/c mice were infected with *M. tuberculosis* bacilli by the intranasal route. (**A**) *Ex vivo* histopathological examination demonstrating pulmonary granulomas as a result of TB infection induction. Lung tissues obtained from BALB/c mice 4 weeks after infection with *M. tuberculosis* before the subsequent treatment are shown. Hematoxylin and eosin (H&E) staining revealed a lung parenchyma-localized granulomatous inflammatory reaction characterized by multifocal nodular infiltrate with macrophages (light cytoplasm and round or irregular nucleus) and lymphocytes. A high-magnification view of the inset is shown in the middle. Ziehl–Nielsen (ZN, right) staining showed numerous acid-fast bacilli (red) in the lesions. During the subsequent treatment, mycobacterial burdens were monitored throughout the course of infection in the lungs (**B**) and spleens (**C**). The effect of the tested formulation (*i.e.*, **NPs**, **RIF**, and **NPs-RIF**) treatments was determined by assaying the mycobacterial CFUs 4, 8, and 12 days post infection. Formulations were administered at 10 mg/kg. The RIF amount was equivalent to those in both the **RIF** and **NPs-RIF** formulations. Scale bars: 200 µm, 100 µm, and 50 µm. The results are expressed as the means ± SD and were analyzed by ANOVA. Taken from [**P2**].

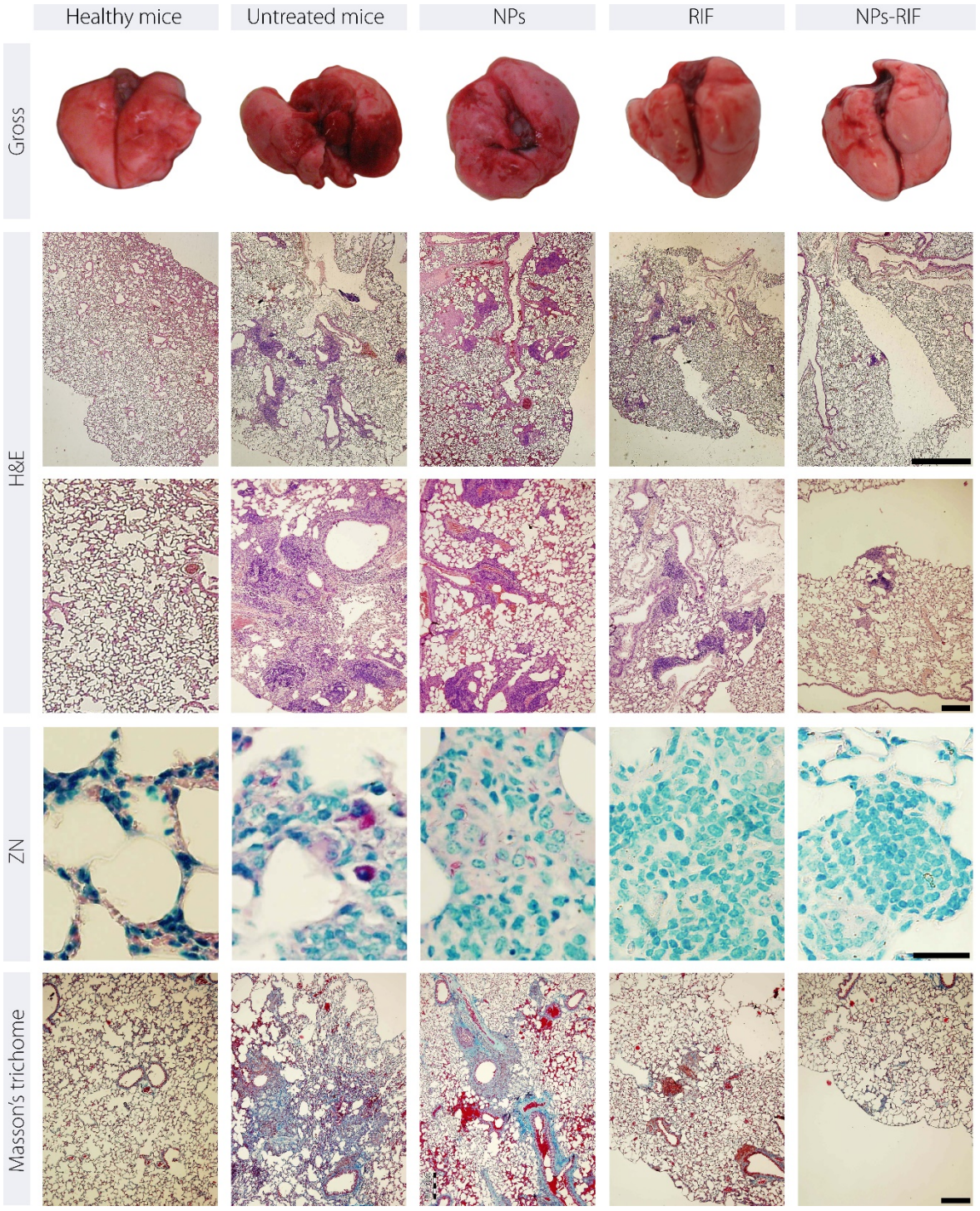

Figure 2.10 *Ex vivo* examination of lung tissue. Twelve weeks after infection, *i.e.*, 8 weeks of treatment, no gross pathology was found. In contrast, hematoxylin and eosin (H&E) staining revealed clear changes in lung parenchyma-localized granulomas as a response to the treatment. The lung tissues demonstrated a marked response to **RIF** and **NPs-RIF** therapy as a clear decrease in collagen deposition (Masson's trichrome staining, blue) and no presence of acid-fast bacilli (ZN staining), whereas lungs dissected from both untreated and **NPs**-treated animals revealed gross fibrosis and numerous acid-fast tubercle bacilli. Scale bars: 1 mm, 200 µm, 25 µm, and 200 µm. Taken from [**P2**].

2.4 Remarks: Mechanism and Enzymatic Degradability

As indicated above, this partial project aimed to comprehensively analyze the effects of a fabricated antitubercular MPEO-*b*-PCL delivery system. The treatment approach conducted as monotherapy showed promising efficacy both on the cellular level and *in vivo*.

Considering the clinical circumstances and safety, it can be suggested that the fabricated nanoformulation is well tolerated, as evident from testing with zebrafish. Moreover, the mice revealed no histopathological changes, and their body weights were maintained over the course of treatment. Considering the mechanism behind the observed efficacy improvement, the three main synergic effects described above can be suggested. First, these include increased bioavailability, prolonged drug release by virtue of the drug being encapsulated in our nanoformulation, and improved critical pharmacokinetic and pharmacodynamic parameters. Second, it can be suggested that after intraperitoneal (in mice) or intravenous (in zebrafish) administration, phagocytes are able to take up the nanobeads and migrate to the site of infection by virtue of chemotaxis. This phenomenon was also described in terms of NP-treated TB[9, 10]. Finally, the Griffiths group[11] described that an enhanced permeability and retention (EPR)-like process, known from antitumor drug delivery systems, occurs, allowing nanobead-based interventions to extravasate from the vasculature to reach granulomas. Since our NPs end up in the systemic circulation, this suggested point is a third possible explanation.

To summarize, the effect of MPEO-*b*-PCL-based nanoparticles carrying rifampicin—a cornerstone of modern antitubercular therapy—on zebrafish infection and lung tuberculosis in mice was described, suggesting that it is an interesting candidate for further investigation.

The advantage of such a system, however, lies also in the fact that it is lipase-degradable by virtue of ester bond hydrolysis. Moreover, as described in publication [**P3**], the enzymatic degradability was found to be controllable by copolymerization with poly(γ-butyrolactone) (P4HB). In this partial work, we compared both MPEO-*b*-PCL and MPEO-*b*-PCL-*co*-P4HB copolymers in terms of enzymatic degradation within living macrophages. This was studied by flow cytometry using DACCA-labeled fluorescent NPs. DACCA is sensitive to changes in the outer environment. Thus, the degradation of DACCA-labeled NPs leads to fluorescence quenching[12]. Based on this analytical approach, it was found that the presence of P4HB in the copolymer matrix reveals faster intracellular degradation. Given this, it is believed that this approach allows for elegant control of biorelevant properties. In other words, the P4HB-containing copolymer MPEO-*b*-PCL-*co*-P4HB reveals a faster degradation rate than the P4HB-free copolymer MPEO-*b*-PCL.

2.5 References

1. Bodratti A.M., Alexandridis P. Amphiphilic Block Copolymers in Drug Delivery: Advances in Formulation Structure and Performance. *Expert Opinion on Drug Delivery*. 2018, 15 (11), 1085–1104.
2. Urbánek T., Jäger E., Jäger A., Hrubý M. Selectively Biodegradable Polyesters: Nature-Inspired Construction Materials for Future Biomedical Applications. *Polymers*. 2019, 11 (6), 1061.
3. Gaucher G., Dufresne M.-H., Sant V.P., Kang N., Maysinger D., Leroux J.-C. Block Copolymer Micelles: Preparation, Characterization and Application in Drug Delivery. *Journal of Controlled Release*. 2005, 109 (1), 169–188.
4. Domingos R.F., Baalousha M.A., Ju-Nam Y., Reid M.M., Tufenkji N., Lead J.R., et al. Characterizing Manufactured Nanoparticles in the Environment: Multimethod Determination of Particle Sizes. *Environmental Science & Technology*. 2009, 43 (19), 7277–7284.
5. Zölls S., Tantipolphan R., Wiggenhorn M., Winter G., Jiskoot W., Friess W., et al. Particles in Therapeutic Protein Formulations, Part 1: Overview of Analytical Methods. *Journal of Pharmaceutical Sciences*. 2012, 101 (3), 914–935.
6. van Leeuwen L.M., van der Sar A.M., Bitter W. Animal Models of Tuberculosis: Zebrafish. *Cold Spring Harbor Perspectives in Medicine*. 2014, 5 (3), a018580–a018580.
7. Davis J.M., Clay H., Lewis J.L., Ghori N., Herbomel P., Ramakrishnan L. Real-Time Visualization of Mycobacterium-Macrophage Interactions Leading to Initiation of Granuloma Formation in Zebrafish Embryos. *Immunity*. 2002, 17 (6), 693–702.
8. Cronan Mark R., Beerman Rebecca W., Rosenberg Allison F., Saelens Joseph W., Johnson Matthew G., Oehlers Stefan H., et al. Macrophage Epithelial Reprogramming Underlies Mycobacterial Granuloma Formation and Promotes Infection. *Immunity*. 2016, 45 (4), 861–876.
9. Dannenberg A.M. Macrophage Turnover, Division and Activation Within Developing, Peak and "Healed" Tuberculous Lesions Produced in Rabbits by BCG. *Tuberculosis*. 2003, 83 (4), 251–260.
10. Fenaroli F., Westmoreland D., Benjaminsen J., Kolstad T., Skjeldal F.M., Meijer A.H., et al. Nanoparticles as Drug Delivery System against Tuberculosis in Zebrafish Embryos: Direct Visualization and Treatment. *ACS Nano*. 2014, 8 (7), 7014–7026.
11. Fenaroli F., Repnik U., Xu Y., Johann K., Van Herck S., Dey P., et al. Enhanced Permeability and Retention-Like Extravasation of Nanoparticles From the Vasculature Into Tuberculosis Granulomas in Zebrafish and Mouse Models. *ACS Nano*. 2018, 12 (8), 8646–8661.
12. Trousil J., Filippov S.K., Hrubý M., Mazel T., Syrová Z., Cmarko D., et al. System With Embedded Drug Release and Nanoparticle Degradation Sensor Showing Efficient Rifampicin Delivery Into Macrophages. *Nanomedicine: Nanotechnology, Biology and Medicine*. 2017, 13 (1), 307–315.

CHAPTER 3: GRAFT COPOLYMER INVESTIGATION

Compared with block copolymers, graft copolymers offer a different method for amphiphilic NP preparation, with less predictability of the behavior. This is probably due to the changes in the polymer backbone flexibility and steric constraints of hydrophobic segments of variable length and grafting density—so indicating that the self-assembly aspects are worth studying. In collaboration with the Sosnik group, we focused on two appealing hydrophilic polymers, poly(vinyl alcohol) (PVA) and chitosan (CS), both of which are mucoadhesive, biocompatible, and widely used as biomaterials[1].

Our strategy lies in the hydrophobization of both PVA and CS with poly(methyl methacrylate) (PMMA) grafts as a model of hydrophobizing polymer [**P4**, **P5**]. Note that the study of mucoadhesive polymers was not accidental—given the aspects of pulmonary infection diseases, it is of interest to study lung drug delivery. The respiratory tract represents a relatively complex system consisting of the upper and lower tracts; the lower tract is tree-analogically branched. The trachea, the largest tube, is branched off into two tubes that branch into secondary and tertiary bronchi; they are further branched into bronchioles. Millions of alveoli, vascularized hollow cup-shaped cavities, are located sparsely on bronchioles. The lungs have a large and highly absorptive surface area of approximately 100 m^2, making the lungs an interesting site of administration[2, 3]. Moreover, a mucus barrier protects the airways by way of discontinuous layer forming[4, 5]. Mucins are a family of high molecular weight anionic cysteine-rich glycoproteins. Drug delivery systems possessing mucoadhesivity thus capitalize on this feature to improve the pharmacodynamics and pharmacokinetics by way of the prolonged residence time of drugs and increased local bioavailability[6]. Hence, the objective of this collaborative study was to characterize poly(vinyl alcohol)-*graft*-poly(methyl methacrylate) (PVA-*g*-PMMA) and chitosan-*graft*-poly(methyl methacrylate) (CS-*g*-PMMA) in terms of self-assembly, colloidal properties and physical stabilization by way of crosslinking.

Below, a commented summary focused on both PVA-*g*-PMMA [**P4**] and CS-*g*-PMMA [**P5**] nanobeads is shown; note that, where mentioned, unpublished results are discussed.

3.1 The PVA story

3.1.1 Self-Assembly and NP Characterization

PVA-based amphiphilic nanobeads were prepared using PVA-*g*-PMMA with M_w and M_n values of 75,000 and 43,000 Da ($Đ$ = 1.74), respectively, as estimated by GPC. The copolymer was synthesized through a free-radical homopolymerization of PMMA on a PVA macroinitiator (**Fig. 3.1A**); detailed characterization of the copolymer obtained in collaboration with the Sosnik group is shown in publication [**P4**].

NP preparation was performed by direct solubilization of the PVA-*g*-PMMA copolymer in water. As suggested above, we studied the preservation of the NP structure by crosslinking PVA domains with boric acid (BA), which is based on the noncovalent stoichiometric 1,3,2-dioxaborinane rings between borate anions and the polyol[7, 8] (stochiometric ratio 2 polyols per 1 borate anion). This leads to anionic complex formation. In the text below, the noncrosslinked and BA-crosslinked samples are referred to as **PVANPs** and **PVANPs-BA**, respectively. The assemblies fabricated were studied using DLS, SLS, ELS, TEM and SANS.

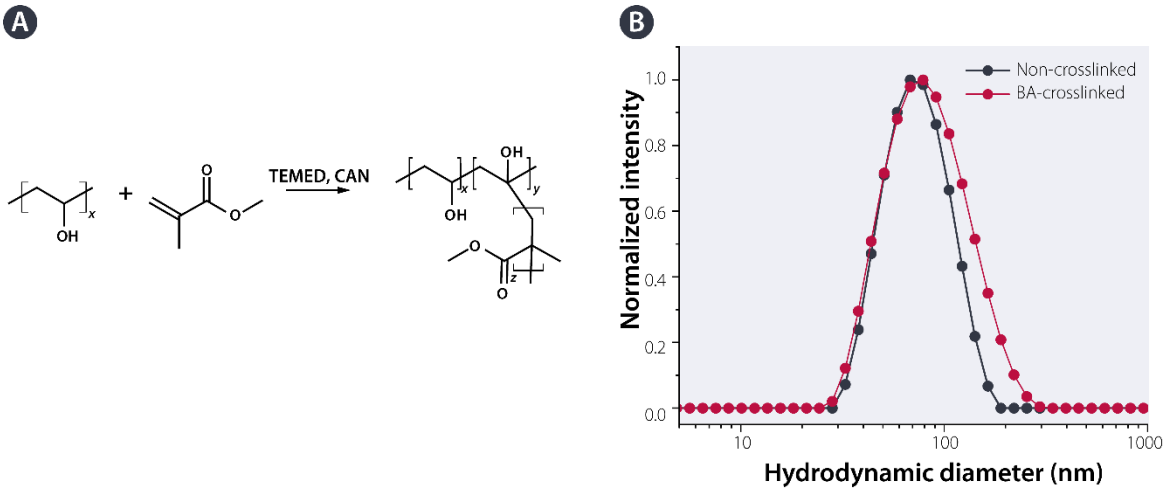

Figure 3.1 Synthesis and self-assembly of the PVA-*g*-PMMA copolymer. (**A**) Scheme of the free radical polymerization in the presence of tetramethylethylenediamine (TEMED) and cerium ammonium nitrate (CAN). (**B**) Size distribution functions as found by DLS. Taken from [**P4**].

Table 3.1 Physicochemical characteristics of the PVA-*g*-PMMA assemblies.

Sample	D_h (nm)[a]	D_g (nm)[b]	M_w^{NPs} (Da)[b]	N_{agg}[b]	d (g/mL)[b]	ζ (mV)[c]
PVANPs	70	77	4.3×10^6	57	0.014	-14.6
PVANPs-BA	74	78	4.4×10^6	63	0.014	-15.5

[a] Determined by DLS.
[b] Determined by SLS.
[c] Determined by electrophoretic light scattering (ELS)
Taken from [**P4**].

The PMMA-hydrophobized PVA is, in principle, an amphiphilic copolymer; it was not, thus, surprising that direct solubilization of the PVA-*g*-PMMA copolymer leads to spontaneous self-association and the formation of light-scattering method-detectable NPs. The samples possessed an overall negative zeta potential (**Table 3.1**), which is in line with results published elswhere[9, 10]. The DLS distribution function of **PVANPs** was found to be portrayed as a relatively narrow mode with a hydrodynamic diameter of approximately 70 nm (**Fig. 3.1B** and **Table 3.1**). When the sample was crosslinked, a slight increase in hydrodynamic diameter (to approximately 74 nm) was observed in the case of **PVANPs-BA**. This may indicate that the crosslinking occurred mainly via intra- and not interparticle routes.

Using SLS, D_g was found to be approximately 80 nm. The aggregation number (N_{agg}) of the particles was calculated according to the following formula:

$$N_{agg} = \frac{M_w^{NPs}}{M_w}, \tag{9}$$

where M_w is the GPC-determined molecular weight of the copolymer and M_w^{NPs} is the molecular weight of the nanoparticles, as determined by SLS. It is evident that both the M_w and N_{agg} of the assemblies increased slightly after crosslinking (**Table 3.1**). The apparent structural density d was calculated according to the following formula:

$$d = \frac{6M_w^{NPs}}{\pi N_A D_{geom}^3}, \tag{10}$$

where N_A is Avogadro's constant and D_{geom} is the geometrical dimension (diameter) calculated as $D_{geom} = 1.29 \cdot D_g$, was found to be reasonably low (0.014 g/cm^3 for both samples). This suggests that the assemblies are most likely water-swollen, even when the particles were crosslinked. The D_g/D_h ratio, a measure of the distribution of the matrix through the nanobead, decreased from 1.10 to 1.05 when the nanobeads were crosslinked, indicating that the **PVANPs-BA** beads are more compact and have less dangling chains than the **PVANPs**. Note that homogenous spheres exhibit a D_g/D_h ratio of 0.775[11]. Thus, the ratios found in this study suggest that the nanobeads represent swollen structures. Overall, the DLS and SLS measurements suggest that BA crosslinking stabilizes the particles and does not lead to any significant density change within the PVA-*g*-PMMA nanobeads. Zeta potential estimation revealed a slight decrease in the case of PVANPs-BA, probably due to the formation of a negatively charged borate complex.

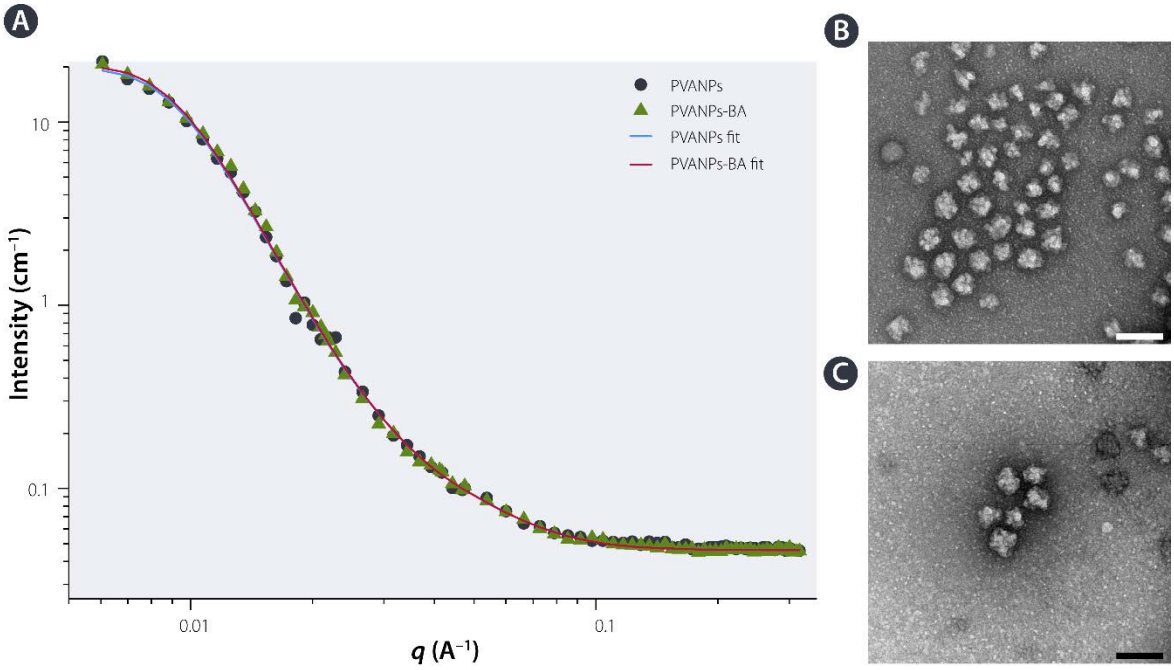

Figure 3.2 Structural analysis of PVA-*g*-PMMA beads. (**A**) SANS patterns and fitting. TEM micrographs of (**B**) **PVANPs** and (**C**) **PVANPs-BA** obtained by conventional TEM with negative staining. Scale bars: 100 nm. Taken from [**P4**].

Similar to the previous story, we combined SANS and TEM to shed light on the assembly size and structure; **Fig. 3.2** depicts both the SANS data and TEM images. Using a Beaucage model that is based on a population of small particles together with larger particles, or conversely, small architectures clustered into large multimicellar structures, the sizes found at 25 °C were D_g = 12 nm and D_g = 84 nm for small and large populations, respectively. Considering the TEM microphotographs, it can be concluded that both **PVANPs** and **PVANPs-BA** possess isometric, though nonspherical, shapes (**Fig. 3.2B** and **3.2C**). The nanobeads were found to be formed from small spherical units, probably unimolecular architectures, with a size of approximately 12–15 nm, assembling into clusters with sizes of 50–60 nm in diameter, which is in relatively good agreement with other results.

Note that SANS investigations revealed an exceptional stability for both **PVANPs** and **PVANPs-BA** at 25, 35, and 40 °C. (**Fig. 3.3A** and **3.3B**), suggesting that this system should also be stable at 37 °C in biological environments.

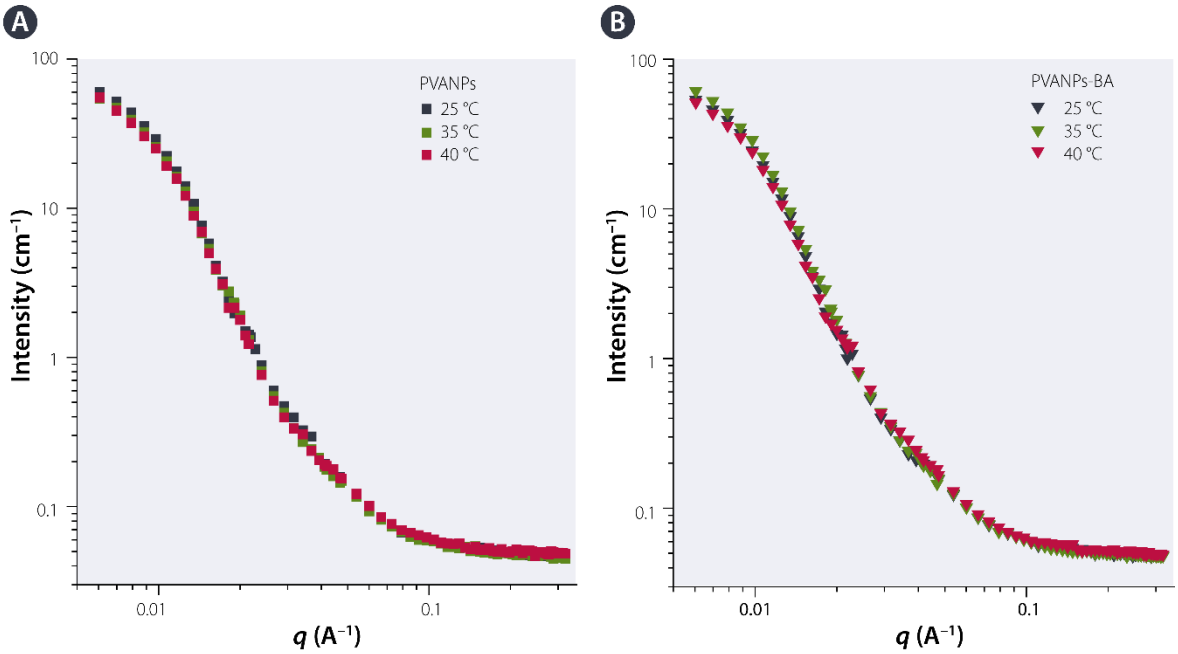

Figure 3.3 Small-angle neutron scattering (SANS) patterns. The experiment was carried out at different temperatures using both **PVANPs** (**A**) and **PVANPs-BA** (**B**). Note that the change in temperature revealed no significant change in the scattering patterns. Taken from [**P4**].

3.2 The CS story

3.2.1 Self-Assembly and NP Characterization

The CS-based amphiphilic nanobeads were prepared using CS-*g*-PMMA with M_w and M_n of 11,000 and 8,700 Da ($Đ$ = 1.26), respectively, as estimated by GPC. Similarly, the copolymer was synthesized through free-radical homopolymerization of PMMA on a CS macroinitiator (**Fig. 3.4A**). Similarly, detailed characterization of the copolymer obtained in collaboration with the Sosnik group can be found in publication [**P5**]. The self-assembly was carried out using the solution casting method comprising cosolubilization of a drug and the copolymer in the same solvent (namely, DMSO), freeze-drying, and direct solubilization in water[12]. Similar to the above-described study with PVA, the physical stabilization of such assemblies was studied; we used ionotropic crosslinking by tripolyphosphate (TPP), which is based on the interaction between the hydrated amino groups ($–NH_3^+$) and the polyanion[13]. The noncrosslinked and TPP-crosslinked nanobeads were referred to as **CSNPs** and **CSNPs-TPP**, respectively.

First, we carried out light scattering analysis to obtain information about the size, zeta potential and size distribution of the fabricated samples. It was proven that direct solubilization of the CS-*g*-PMMA copolymer leads to the formation of nanoarchitectures with an overall positive charge owing to the $–NH_3^+$ side-chain groups of CS. Crosslinking by TPP led to a decrease in the zeta potential from approximately +42 mV to approximately 22 mV. This was probably due to the partial neutralization of the positively charged groups (**Table 3.2**). As depicted in **Fig. 3.4B**, the DLS distribution function of the **CSNP** dispersion is portrayed as a relatively broad peak. This suggests that the dispersions are based on a number of size populations. The hydrodynamic diameter (D_h) was found to be 188 nm (**Table 3.2**). **CSNPs-TPP** revealed a broad distribution function with a D_h value of 134 nm.

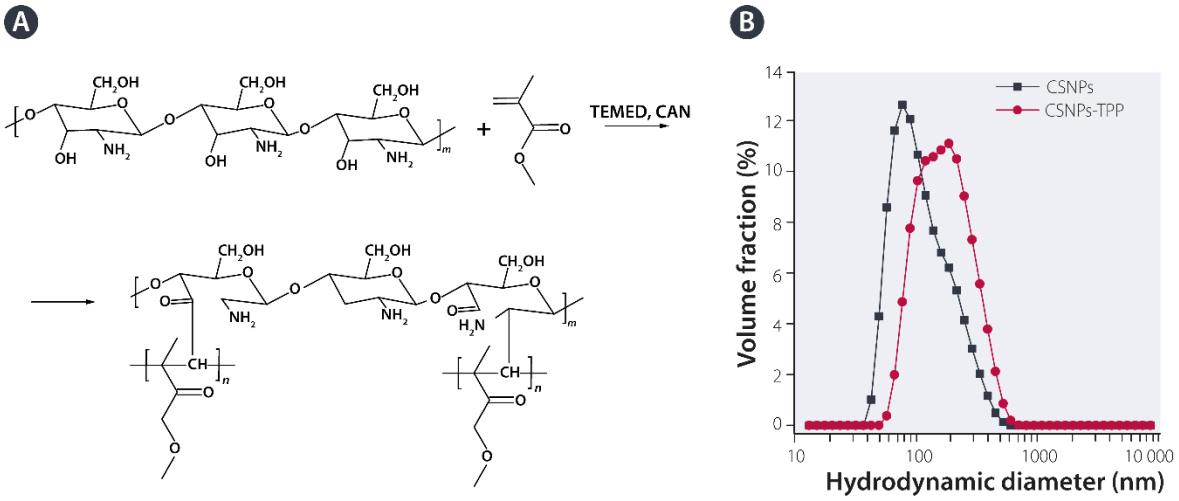

Fig. 3.4 Synthesis and self-assembly of the CS-*g*-PMMA copolymer. (**A**) Scheme of the free radical polymerization in the presence of tetramethylethylenediamine (TEMED) and cerium ammonium nitrate (CAN). (**B**) Size distribution functions as found by DLS. Taken from [**P5**].

Table 3.2 Characterization of CS-g-PMMA nanoparticles by DLS and SLS.

Sample	D_h (nm)[a]	D_g (nm)[b]	M_w^{NPs} (g/mol)[b]	d (g/mL)[c]	N_{agg}[c]	ζ (mV)
CSNPs	188	212	5.0×10^6	0.002	455	+42
CSNPs-TPP	134	168	7.1×10^7	0.11	6455	+22

[a] Measured by DLS.
[b] Measured by SLS.
[c] Values obtained from GPC and SLS were used for the calculation.
Taken from [**P5**].

SLS investigations revealed D_g values of 212 and 168 nm for **CSNPs** and **CSNPs-TPP**, respectively. The D_g/D_h ratio is often used as a measure of the material distribution through the particle. As mentioned in Chapter 1, for monodisperse hard spheres, the D_g/D_h ratio is equal to 0.775[14]. The D_g/D_h ratio found is equal to 1.12 for **CSNPs** and 1.31 for **CSNPs-TPP**. As could be expected, the higher value for the **CSNPs-TPP** indicates a smaller contribution of loose chains in the surface crosslinking. This is also reflected in the lower value of D_h observed in the case of **CSNPs-TPP**. This also suggests that both kinds of particles represent highly swollen structures. In other words, the nanobead volume is filled with water, as suggested by the apparent structural density values calculated according to Eq. 10.

To obtain a more detailed picture of the **CSNPs** and **CSNPs-TPP** samples, SANS and TEM investigations were carried out. Normalized SANS data for both **CSNPs** and **CSNPs-TPP** are depicted in **Fig. 3.5A**. Given the SANS curve fitting performed, it is evident that a simple Guinier analysis did not provide a proper fit (dashed curve). The shape of the SANS curves (*i.e.*, a small plateau in the medium q-range and start of a plateau in the lowest q-range) could suggest the presence of at least two sizes. In other words, a population of small particles together with larger particles, or conversely, small architectures clustered into larger multimicellar structures, can be present. Using the Beaucage model, a small population of $D_g = 10$ nm and a large population of $D_g = 76$ nm were found. Assuming that these values represent spherical architectures, one can calculate the corresponding diameter from the following equation:

$$D_g = \frac{3}{5} D^2 \,, \tag{11}$$

resulting in values of approximately 13 nm and 98 nm. The results were the same for both samples. It is not, however, possible to state whether the small size population corresponds to free CS-*g*-PMMA copolymer or, as indicated by TEM (see below), to building blocks.

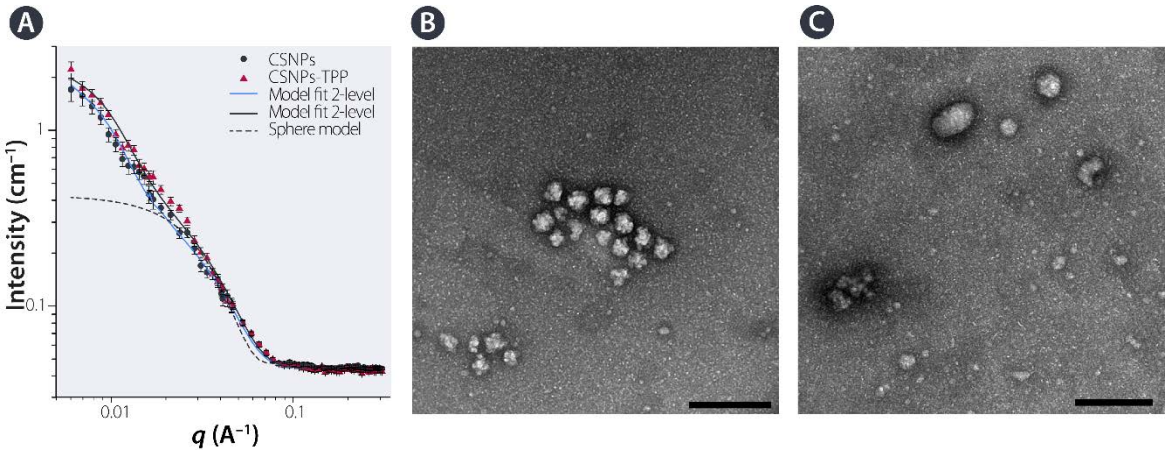

Figure 3.5 Structural analysis of CS-*g*-PMMA assemblies. (**A**) SANS patterns and fitting. TEM micrographs of (**B**) **CSNPs** and (**C**) **CSNPs-TPP** obtained by TEM with negative staining. Scale bars: 200 nm. Taken from [**P5**].

TEM micrographs are depicted in **Fig. 3.5B** and **3.5C**. The **CSNP** sample revealed a major population of spherical-like assemblies with a size of approximately 40–50 nm, together with a small fraction of particles having a size of 6–10 nm that seems to agree well the presence of unimolecular assemblies, as found by the negative staining with uranyl acetate. The results found were in line with the SANS analysis and suggested that the CS-*g*-PMMA copolymer presents a complex self-association pattern. Smaller particles were found within both **CSNPs** and **CSNPs-TPP** samples; larger particles in the **CSNPs-TPP** sample had similar sizes as those found for **CSNPs**; however, their structure was more compact. This is in line with the increase in apparent structural density (**Table 3.1**). Note that a certain fraction of the **CSNPs-TPP** formed even larger architectures (approximately 100–200 nm in diameter), as evident from the TEM investigations.

Similar to the PVA story, SANS investigation was also conducted at different temperatures, and in general, the assemblies revealed good temperature stability due to the low thermoresponsiveness of the components (**Fig. 3.6**).

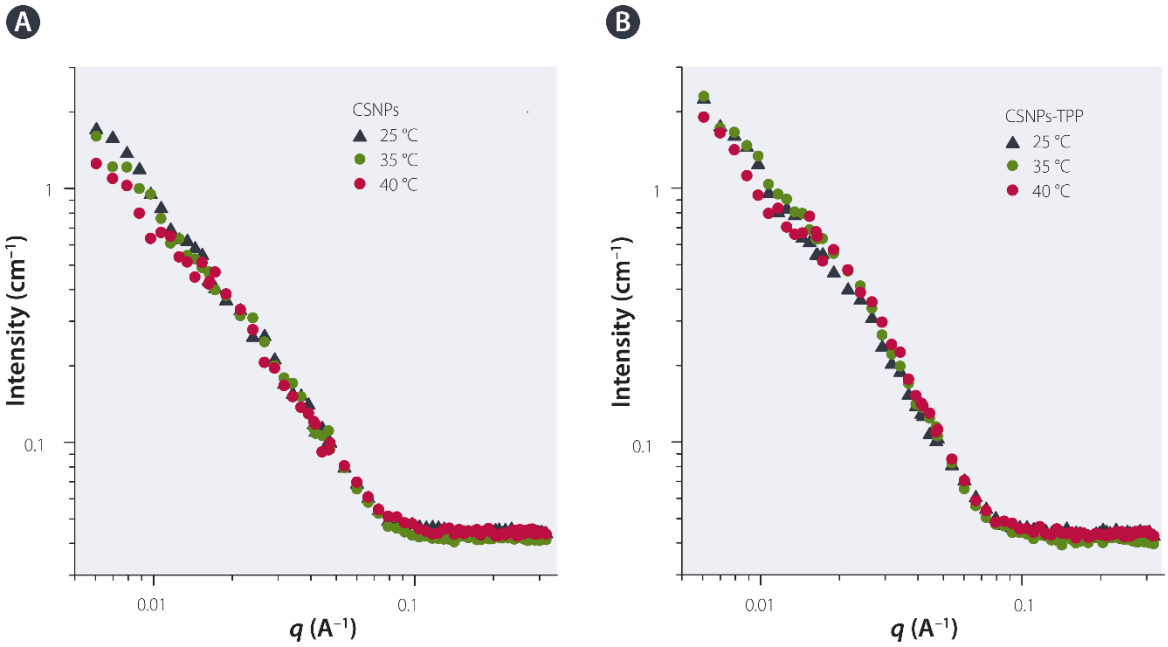

Figure 3.6 Small-angle neutron scattering (SANS) patterns. The experiment was carried out at different temperatures using both **CSNPs** (**A**) and **CSNPs-TPP** (**B**). Note that the change in temperature revealed no significant change in the scattering patterns. Taken from [**P5**].

3.3 References

1. Teodorescu M., Bercea M., Morariu S. Biomaterials of Poly(vinyl alcohol) and Natural Polymers. *Polymer Reviews*. 2018, 58 (2), 247–287.
2. Patwa A., Shah A. Anatomy and Physiology of Respiratory System Relevant to Anaesthesia. *Indian Journal of Anaesthesia*. 2015, 59 (9), 533–541.
3. Huang Y.Y., Wang C.H. Pulmonary Delivery of Insulin by Liposomal Carriers. *Journal of Controlled Release*. 2006, 113 (1), 9–14.
4. Patil J.S., Sarasija S. Pulmonary Drug Delivery Strategies: A Concise, Systematic Review. *Lung India*. 2012, 29 (1), 44–49.
5. Ridley C., Thornton D.J. Mucins: The Frontline Defence of the Lung. *Biochemical Society Transactions*. 2018, 46 (5), 1099–1106.
6. Boegh M., Foged C., Müllertz A., Mørck Nielsen H. Mucosal Drug Delivery: Barriers, in Vitro Models and Formulation Strategies. *Journal of Drug Delivery Science and Technology*. 2013, 23 (4), 383–391.
7. Itou T., Kitai H., Shimazu A., Miyazaki T., Tashiro K. Clarification of Cross-Linkage Structure in Boric Acid Doped Poly(vinyl alcohol) and Its Model Compound As Studied by an Organized Combination of X-ray Single-Crystal Structure Analysis, Raman Spectroscopy, and Density Functional Theoretical Calculation. *The Journal of Physical Chemistry B*. 2014, 118 (22), 6032–6037.
8. Jia Y., Bai S., Park C.B., Wang Q. Effect of Boric Acid on the Foaming Properties and Cell Structure of Poly(vinyl alcohol) Foam Prepared by Supercritical-CO2 Thermoplastic Extrusion Foaming. *Industrial & Engineering Chemistry Research*. 2017, 56 (23), 6655–6663.
9. Thorat N.D., Shinde K.P., Pawar S.H., Barick K.C., Betty C.A., Ningthoujam R.S. Polyvinyl Alcohol: An Efficient Fuel for Synthesis of Superparamagnetic LSMO Nanoparticles for Biomedical Application. *Dalton Transactions*. 2012, 41 (10), 3060–3071.
10. Sahoo S.K., Panyam J., Prabha S., Labhasetwar V. Residual Polyvinyl Alcohol Associated With Poly(D,L-lactide-co-glycolide) Nanoparticles Affects Their Physical Properties and Cellular Uptake. *Journal of Controlled Release*. 2002, 82 (1), 105114.
11. Santos N.C., Sousa A.M.A., Betbeder D., Prieto M., Castanho M.A.R.B. Structural Characterization of Organized Systems of Polysaccharides and Phospholipids by Light Scattering Spectroscopy and Electron Microscopy. *Carbohydrate Research*. 1997, 300 (1), 31–40.
12. Gaucher G., Dufresne M.-H., Sant V.P., Kang N., Maysinger D., Leroux J.-C. Block Copolymer Micelles: Preparation, Characterization and Application in Drug Delivery. *Journal of Controlled Release*. 2005, 109 (1), 169–188.
13. Sreekumar S., Goycoolea F.M., Moerschbacher B.M., Rivera-Rodriguez G.R. Parameters Influencing the Size of Chitosan-TPP Nano- and Microparticles. *Scientific Reports*. 2018, 8 (1), 4695.
14. Varga I., Gilányi T., Mészáros R., Filipcsei G., Zrínyi M. Effect of Cross-Link Density on the Internal Structure of Poly(N-isopropylacrylamide) Microgels. *Journal of Physical Chemistry B*. 2001, 105 (38), 9071–9076.

CHAPTER 4: SUMMARY AND FUTURE PERSPECTIVES

4.1 Overall Summary

Polymeric nanobead-based interventions represent a favorite and emerging group of drug delivery systems[1]. In this thesis, polymeric nanobeads based on both block and graft amphiphilic copolymers were engineered, analyzed, and evaluated in the context of intracellular infections. This research was motivated by the shortcomings of conventional antibacterial interventions. Due to the inefficacies of current therapies, there is an unmet need for rapid diagnostic improvements and novel strategies for interventions dealing with the physicochemical, pharmacokinetic, and pharmacodynamic obstacles related to conventional treatment. This research interest led to the goal of designing, fabricating, and comprehensively analyzing a drug delivery system capable of promoting intracellular drug delivery and sequentially bearing intracellular bacteria.

In Chapter 2, we described a system based on MPEO-*b*-PCL block copolymer NPs loaded with a model antitubercular agent—rifampicin. The copolymer was synthesized through ring-opening polymerization. As the aim of this work was to understand the properties of such NPs and how they behave in biological environments, they were subjected to robust physicochemical characterization and biorelevant analysis. When we studied the interaction of this intervention with cells, it was found that they possess excellent properties in terms of cytotoxicity, cellular uptake, and antimycobacterial activity *in vitro*. Importantly, the enzymatic degradability of the MPEO-*b*-PCL-based beads is controllable by means of 4HB incorporation. Using a murine model, we demonstrated that the drug-loaded NPs possess improved pharmacokinetic and pharmacodynamic parameters. Ultimately, using two animal models, we were able to study the antitubercular efficacy *in vivo*. This experimental approach and the observations are unique, as handling with bacterial pathogens requires specific biosafety facilities. Overall, this study provides a generalizable strategy for the improvement of intracellular infection treatment, and the results obtained have significant implications in the field of biorelevant analysis of nanobead-based interventions.

Despite the fact that intraperitoneally administered RIF formulations provided excellent parameters, one may object that infections such as tuberculosis are localized in the lungs. This justified objection led to the study of mucoadhesive beads that could even increase the treatment of pulmonary diseases by way of prolonged residence time of a drug[2].

In Chapter 3, we focused on the study of the self-assembly behavior of mucoadhesive PVA-*g*-PMMA and CS-*g*-PMMA copolymers, both synthesized by free-radical polymerization. In this work, nanobeads were prepared by direct solubilization in aqueous media, leading to NP formation. The assemblies were then initially inspected by light scattering methods. It is, however, worth stressing here that DLS investigations in most situations cannot measure the actual size distributions of particles; the sizes obtained are usually overestimated[3, 4]. For this reason, similar to the MPEO-*b*-PCL story, we used several complementary analytical instrumental tools, such as DLS, SLS, SANS, and TEM, to shed light on the nanoarchitecture of such nanobeads. Using this combined approach, we found that both the PVA-*g*-PMMA and CS-*g*-PMMA nanobeads exhibit a complex self-assembled hierarchical structure based on smaller particles associated with larger species. With respect to the prediction of biological activity, one may suggest that the NP size range observed is suitable for internalization into both macrophages and epithelial cells[5]. An important drawback of self-assembled colloids is their low physical stability upon profuse dilution[6, 7]. This in the biological environment may

result in the release of the active cargo within an off-target body site. Thus, we also studied the formation of stabilized amphiphilic NPs by crosslinking. Overall, this study opens new horizons towards the application of self-assembled nanobeads, particularly as drug delivery platforms.

4.2 Challenges and Future Directions

The work discussed in this thesis presents a comprehensive in-depth study of nanobead-based interventions for the treatment of intracellular infections. It is, however, worth stressing that there is much left to be explored and investigated and that there are still essential questions related to this issue that are not fully answered or managed. This resulted in two overview publications [**P6**, **P7**]. The following portion of this chapter will delve into possible future directions towards improving polymer-based treatments for intracellularly persisting infections.

Demonstrations showing that nanobead-based interventions have greater *in vitro* and *in vivo* therapeutic efficacy than the free drug is an important proof of principle. Studies of additional drug incorporation and rational design features have the potential for even greater improvements in efficiency for the therapy of different types of persistent bacterial infections. As suggested above, there are still dozens of questions related to this emerging field of nanomedicine. For instance, comprehensive addressing of the NPs' corona modification effects, different stimulus responsivities and their effect on intracellular infections, and the comparison of drug entrapment methods (encapsulated *vs.* conjugated antibiotics) are needed, and such results may be expected to further enhance the efficacy of novel antibacterial interventions based on nanomedicines. It is claimed that comprehensive investigation and toxicity studies of novel and promising "future medicines" are missing and thus increase the final cost of a novel intervention[8]. Overall, there is always a need for financial support and further preclinical studies to move on to the next developmental step and reach patients. Similarly, inhaled therapy may hold the key for improved interventions in this context. Unfortunately, there is no completed clinical study, and it is difficult to identify which system and which approach would be the most advantageous to pursue.

When addressing TB, one of the major complications is the selection of *M. tuberculosis* strains possessing multidrug-resistant (defined as resistance to both RIF and isoniazid) and extensively drug-resistant (defined as resistance to at least one second-line injectable drug and any fluoroquinolone drug) characteristics. In terms of conventional therapy, multidrug regimens are therefore necessary to reduce the population of mycobacteria to undetectable levels and to avoid the selection of resistant strains[9]. One may thus point out that an important task in the field of TB involves the fabrication of nanomedicines based on cocktail therapy. For instance, Sato and colleagues[10] fabricated micelle-forming prodrugs based on poly(ethylene oxide)-*block*-poly(aspartic acid) covalently modified by RIF, isoniazid and pyrazinamide. Similarly, the Ma group[11] described bovine serum albumin NPs loaded with both isoniazid and RIF. Unfortunately, papers dealing with mono-anti-TB delivery still dominate, probably because anti-TB agents possess different acido-basic properties as well as lipophilicity. An interesting strategy may lie in the combination of nanomedicines with immunotherapy for vaccine delivery, an approach that can increase the therapeutic response of the host. For example, Dube and colleagues[12] fabricated an immunomodulating system for intracellular RIF delivery based on 1,3-β-glucan-functionalized PLGA nanoparticles with a chitosan shell. Chitosan nanocarriers were recently studied by Tailleux[13]. By comparing the transcriptional profiles of untreated macrophages with those incubated with CS nanobeads, 242 genes for which the expression was modulated by CS were identified. In particular, inflammation- and chemokine-related genes were strongly upregulated, as proven by enzyme-linked immune sorbent assay (ELISA). One may hypothesize that the described CS-*g*-PMMA nanobeads may possess immunomodulating properties as well and take advantage of the CS-related effects mentioned. This should, however, be addressed further in the future.

In addition to the development of novel interventions, rapid diagnostic improvements are urgently needed[14]. For example, the causative agent of TB grows very slowly in culture. Obtaining visible colonies on cultivation plates requires weeks of incubation. Thus, in addition to the focus on "future medicines", it is necessary to develop rapid, sensitive and specific diagnostic and bioanalytical methods, as only early diagnosis and therapy significantly reduce the risk of further spread. As reviewed in [**P7**], optical methods using fluorescence and bioluminescence are especially valuable for the imaging, probing, and analysis of mycobacterial infections both *in vitro* and *in vivo*. These tools were found to be useful for the study of the fate and efficiency of drug delivery systems and, thus, important for further research. Dealing with bacterial pathogens will, however, complicate the development of novel interventions, as most intracellular bacteria are highly virulent agents, and handling them requires specific biosafety facilities.

To conclude, in today's world, the risk of untreatable infections is ever present, making the suggested questions and challenges of utmost importance.

4.3 References

1. Lim Y.H., Tiemann K.M., Hunstad D.A., Elsabahy M., Wooley K.L. Polymeric Nanoparticles in Development for Treatment of Pulmonary Infectious Diseases. *Wiley interdisciplinary reviews Nanomedicine and nanobiotechnology*. 2016, 8 (6), 842–871.
2. Vieira A.C.C., Chaves L.L., Pinheiro S., Pinto S., Pinheiro M., Lima S.C., et al. Mucoadhesive Chitosan-Coated Solid Lipid Nanoparticles for Better Management of Tuberculosis. *International Journal of Pharmaceutics*. 2018, 536 (1), 478–485.
3. Domingos R.F., Baalousha M.A., Ju-Nam Y., Reid M.M., Tufenkji N., Lead J.R., et al. Characterizing Manufactured Nanoparticles in the Environment: Multimethod Determination of Particle Sizes. *Environmental Science & Technology*. 2009, 43 (19), 7277–7284.
4. Zölls S., Tantipolphan R., Wiggenhorn M., Winter G., Jiskoot W., Friess W., et al. Particles in Therapeutic Protein Formulations, Part 1: Overview of Analytical Methods. *Journal of Pharmaceutical Sciences*. 2012, 101 (3), 914–935.
5. Gustafson H.H., Holt-Casper D., Grainger D.W., Ghandehari H. Nanoparticle Uptake: The Phagocyte Problem. *Nano Today*. 2015, 10 (4), 487–510.
6. Owen S.C., Chan D.P.Y., Shoichet M.S. Polymeric Micelle Stability. *Nano Today*. 2012, 7 (1), 53–65.
7. Patist A., Kanicky J., Shukla P., Shah D. Importance of Micellar Kinetics in Relation to Technological Processes. *Journal of Colloid and Interface Science*. 2002, 245, 1–15.
8. Grotz E., Tateosian N., Amiano N., Cagel M., Bernabeu E., Chiappetta D.A., et al. Nanotechnology in Tuberculosis: State of the Art and the Challenges Ahead. *Pharmaceutical Research*. 2018, 35 (11), 213.
9. Zumla A., Nahid P., Cole S.T. Advances in the Development of New Tuberculosis Drugs and Treatment Regimens. *Nature Reviews Drug Discovery*. 2013, 12 (5), 388–404.
10. Silva M., Ferreira E., Leite C., Sato D. Preparation of Polymeric Micelles for Use as Carriers of Tuberculostatic Drugs. *Tropical Journal of Pharmaceutical Research*. 2007, 6 (4), 815–824.
11. Ge Z., Ma R., Xu G., Chen Z., Zhang D., Wang Q., et al. Development and In Vitro Release of Isoniazid and Rifampicin-Loaded Bovine Serum Albumin Nanoparticles. *Medical Science Monitor*. 2018, 24, 473–478.
12. Dube A., Reynolds J.L., Law W.-C., Maponga C.C., Prasad P.N., Morse G.D. Multimodal Nanoparticles That Provide Immunomodulation and Intracellular Drug Delivery for Infectious Diseases. *Nanomedicine: Nanotechnology, Biology and Medicine*. 2014, 10 (4), 831–838.
13. Coya J.M., De Matteis L., Giraud-Gatineau A., Biton A., Serrano-Sevilla I., Danckaert A., et al. Tri-Mannose Grafting of Chitosan Nanocarriers Remodels the Macrophage Response to Bacterial Infection. *Journal of Nanobiotechnology*. 2019, 17 (1), 15–15.
14. Srivastava S., Singh P.K., Vatsalya V., Karch R.C. Developments in the Diagnostic Techniques of Infectious Diseases: Rural and Urban Prospective. *Advances in Infectious Diseases*. 2018, 8 (3), 121–138.

PUBLICATIONS ATTACHED

P1 **Trousil J.**, Syrová Z., Dal N. K., Rak D., Konefał R., Pavlova E., Matějková J., Cmarko D., Kubíčková P., Pavliš O., Urbánek T., Sedlák M., Fenaroli F., Raška I., Štěpánek P., Hrubý M. *Biomacromolecules*. 2019, 20 (4), 1798–1815. IF = 5.67

P2 **Trousil J.**, Pavliš O., Kubíčková P., Dai Y.-S., Škorič M., Marešová V., Knudsen D. K., Pavlova E., Fang J.-Y., Zimmerman M., Dartois V., Hrubý M. *Journal of Controlled Release*. 2020. 321, 312–323. IF = 7.90

P3 Urbánek T., **Trousil J.**, Rak D., Gunár K., Konefał R., Šlouf M., Sedlák M., Šebestová J. O., Hrubý M. γ-Butyrolactone copolymerization with the well-documented polymer drug carrier poly(ethylene oxide)-*block*-poly(ε-caprolactone) to fine-tune its biorelevant properties. *Macromolecular Bioscience*. 2020, 1900408. IF = 3.85

P4 Halamish M. H., **Trousil J.**, Rak D., Knudsen D. K., Pavlova E., Nyström B., Štěpánek P., Sosnik A. Self-assembly and nanostructure of poly(vinyl alcohol)-*graft*-poly(methyl methacrylate) amphiphilic nanoparticles. *Journal of Colloid and Interface Science*. 2019, 553, 512–523. IF = 6.36

P5 Schlachet I., **Trousil J.**, Rak D., Knudsen D. K., Pavlova E., Nyström B., Sosnik A. Chitosan-*graft*-poly(methyl methacrylate) amphiphilic nanoparticles: Self-association and physicochemical characterization. *Carbohydrate polymers*. 2019, 212, 412–420. IF = 6.04

P6 **Trousil J.**, Hrubý M. Novel nanoparticle delivery systems for rifampicin: an effective strategy against tuberculosis? *Nanomedicine (Lond.)*. 2017, 12 (12), 1359–1361. IF = 5.00

P7 **Trousil J.**, Ulmann V., Hrubý M. Fluorescence and bioluminescence in the quest for imaging, probing and analysis of mycobacterial infections. *Future Microbiology*. 2018, 13 (8), 933–951. IF = 3.19